Multiaxial deformations of ionic polymer metal composites

Alain Boldini[a], Maurizio Porfiri[a,b,*]

[a] *Department of Mechanical and Aerospace Engineering, Tandon School of Engineering, New York University, Brooklyn, New York 11201, USA*
[b] *Department of Biomedical Engineering, Tandon School of Engineering, New York University, Brooklyn, New York 11201, USA*

Abstract

Ionic polymer metal composites (IPMCs) are a promising class of soft active materials. Their high compliance, low actuation voltage, and ability to operate in wet environments have motivated two decades of intensive research on IPMC actuators. While we have witnessed several breakthroughs in the technology of IPMCs, from additive manufacturing of IPMCs to IPMC-based robots, our understanding of the physical underpinnings of their actuation remains elusive. There is a paucity of continuum physically-based models to investigate IPMC actuation, where the literature relies on structural models that postulate admissible mechanical deformations from classical beam or plate theories. In this sense, we know little about multiaxial deformations elicited by counterions' diffusion and electromigration through the ionomer. Here, we demonstrate that macroscopic actuation of IPMCs is accompanied by localized mechanical deformations in the vicinity of the electrodes, caused by osmotic pressure and Maxwell stress. Toward this aim, we put forward a comprehensive nonlinear finite element analysis, conducted in Abaqus™ through a newly developed user element that allows for testing hypothesis on the inner workings of IPMC actuation and exploring complex configurations. Alongside with computational advances, we establish an exact solution for the two-dimensional Saint-Venant problem of plane-strain actuation of an IPMC, based on linear elasticity and nonlinear electrochemistry. Verified against finite element results, the exact solution offers a mathematically-tractable treatment of localized phenomena in the vicinity of the electrodes. Our results unveil a rich dependence of through-the-thickness deformation on the electric double layers that are formed in the vicinity of the electrodes. Due to the asymmetry of the boundary layers in the vicinity of the cathode and the anode, the ionomer deforms asymmetrically with respect to its mid-axis that also experiences an axial stretch. The Poisson ratio of the ionomer is found to have a critical role in shaping the response of the IPMC, from the onset of actuation to its back-relaxation. This study constitutes a first modeling step toward illuminating complex, multiaxial deformations of IPMCs, whose understanding is critical toward the design and manufacturing of high performance IPMC actuators.

Keywords: Electrochemistry; Finite element; Maxwell stress; Poisson-Nernst-Planck; Uniform bending

1. Introduction

Ionic polymer metal composites (IPMCs) are an emerging class of soft active materials which hold promise in a number of engineering and scientific domains where highly compliant actuators with low operation voltage for use in wet and dry environments are needed (Shahinpoor, 2015; Jo et al., 2013). Their propitious attributes have fueled intensive research in the design of IPMC actuators for integration in soft robotics, biomedical engineering, flow control, and micro-manipulators (Bhandari et al., 2012; Shahinpoor & Kim, 2004; Chen, 2017). For example, several authors have investigated the design of biologically-inspired propulsors based on IPMCs, from robotic fish (Aureli et al., 2010; Chen et al., 2009) to tadpoles (Kim et al., 2005), manta rays (Chen et al., 2012), flying fish (Stalbaum et al., 2017), and jelly fish (Yeom & Oh, 2009; Najem et al., 2012), opening the door to unprecedented applications in underwater robotics. Recent advancements in rapid prototyping of IPMCs (Carrico et al., 2017) make an even more compelling case for the high potential of these highly-tailorable materials as fundamental building blocks for soft devices.

The progress on IPMC technology has been remarkable, but research on modeling has been scattered. While IPMCs share similarities with classical sandwich structures in aerospace and naval engineering, the complexity of their behavior continues to challenge a full comprehension of their physical underpinnings. To date, there is a general understanding of IPMC physics, but several key phenomena that are unique to these materials are yet to be fully explained by rigorous mathematical modeling. It is presently understood that actuation is related to the diffusion and electromigration of mobile counterions which pile-up toward the cathode and deplete the anode, as a voltage is applied across the electrodes (Shahinpoor, 2015; Jo et al., 2013). Recent experiments by Park et al. (2010) enabled the visualization of this phenomenon through fluorescent microscopy. This charge redistribution has been identified as the main driver of IPMC actuation since the early work of Nemat-Nasser and Li more than fifteen years ago (Nemat-Nasser & Li, 2000), where actuation is described through a spherical residual stress proportional to the charge density. This hypothesis has been used by several authors (Chen & Tan, 2008; Nardinocchi et al., 2011; Porfiri, 2009; Wallmersperger et al., 2007) toward models of IPMC actuation based on reduced-order beam- and plate-like structural theories.

Recently, a thermodynamically-based continuum model of IPMCs has been formulated (Cha & Porfiri, 2014), providing new insight into several open questions in IPMC modeling. In contrast with the state of the art, the model establishes that IPMC actuation is not exclusively determined by the charge density. Both the charge density and the electric field contribute to IPMC actuation, by regulating the interplay between osmotic pressure and Maxwell stress. The model shares similarities with the recent work of Zhu et al. (2013), which also recognizes the importance of electrostatic effects on IPMC actuation, but the

*Corresponding author
Email address: mporfiri@nyu.edu (Maurizio Porfiri)

thermodynamically-based framework of Hong et al. (2010) is used to derive the constitutive response, rather than delving into the microscopy of the ionomer clusters.

Through this continuum model, in Porfiri et al. (2017) the possibility to predict the phenomenon of back-relaxation has been demonstrated, as a result of the nonlinear interplay between Maxwell stress and osmotic pressure. In Porfiri et al. (2018), the analysis has been expanded to account for the presence of high surface electrodes and steric effects toward a more accurate prediction of the onset and extent of back-relaxation as a function of physical and geometric properties. However, the predictions of both Porfiri et al. (2017) and Porfiri et al. (2018) are still based on a structural model of IPMC deformation. More specifically, they rest on the hypothesis that each IPMC cross-section is rigid, within the classical Euler-Bernoulli structural beam theory. Whether this assumption is accurate has never been tested in the literature.

The chief objective of this paper is to critically examine this hypothesis, which, in fact, is pervasive to the entire field of IPMC modeling (Shahinpoor, 2015; Jo et al., 2013). To address this goal, we undertake two major research endeavors. First, we develop a finite element (FE) computer code to simulate the complete nonlinear model in Cha & Porfiri (2014) under plane-strain conditions in two dimensions. The FE solution is derived from first principles, starting from a weak formulation of the model with respect to variations in the displacement field, counterions' concentration, and electric potential. The governing equations are implemented in the commercial FE software Abaqus™ in a user-defined implicit element (UEL) (Chester et al., 2015). The element-level residuals vector and tangents matrix for the Abaqus™ Newton solver are computed in the subroutine using Gauss integration. This computational framework builds on recent efforts that have attempted at the FE simulation of IPMCs (Pugal et al., 2014, 2015). Specifically, Pugal et al. (2014) proposed the use of adaptive high-order finite elements to solve coupled Poisson-Nernst-Planck and Navier equations, and a tutorial for Comsol™ implementation of an analogous set of equations has been recently presented in Pugal et al. (2015). However, the model considered in Pugal et al. (2014, 2015) radically differs from ours in the treatment of the actuation, which is therein phenomenologically described as a bulk force, whose magnitude is proportional to the charge density and whose direction follows the electric field. Related endeavors on the FE analysis of ionic membranes can be found in Rossi & Wallmersperger (2018) and Chen et al. (2018).

Second, we establish an exact linear elasticity solution for the actuation of slender IPMCs in two-dimensions by combining previous work on matched asymptotic expansions (Porfiri, 2008) with the classical Saint-Venant approach to linear elasticity (Timoshenko & Goodier, 2001). Exact elasticity solution of IPMC deformations are unprecedented; our solution allows for a thorough characterization of the multiaxial state of deformation taking place during IPMC actuation. From the voltage applied across the electrodes, we demonstrate the computation of the IPMC electrochemistry and strain fields in terms of measurable physical and geometric parameters. In particular, we put forward a transparent approach to the study of IPMC actuation, in which one solves a simple lumped parameter circuit model (consisting of a single

nonlinear ordinary differential equation) to compute the voltage drop across the electric double layers. From the voltage drop across the double layers, all the salient mechanical and electrochemical fields are then evaluated. The exact solution obtained with this procedure is verified against FE simulations, to assess the validity of the hypotheses of the analytical derivation. More specifically, we determine that nonlinearities may play a significant role on IPMC mechanics for moderate values of voltage applied across the electrodes.

Predictably, we find that IPMC cross-sections do not act as rigid bodies during actuation. While the axial strain follows the typical linear trend of the classical beam theory and the shear strain is negligible, both analytical and FE results bring forward a complex, counter-intuitive deformation through the thickness. More specifically, we observe the formation of two strain boundary layers on the top and bottom surfaces of the ionomer, causing the IPMC to macroscopically contract along its thickness. The deformation is not symmetric with respect to the mid-axis, due to the asymmetry in the charge boundary layers in the vicinity of the electrodes. As a result, the neutral axis, where the axial strain is zero, shifts from the mid-axis toward the anode or the cathode, depending on the level of the applied voltage. These effects are mediated by the Poisson ratio of the ionomer, which, ultimately, plays a remarkable role on IPMC actuation, by modulating the mechanical response from the onset of actuation to the back-relaxation.

The rest of the paper is organized as follows. In Section 2, we briefly review the continuum model proposed in Cha & Porfiri (2014). In Section 3, we introduce our FE scheme for the study of IPMC mechanics and electrochemistry, offering details on the mathematical formulation and numerical implementation. In Section 4, we present our exact solution, detailing its modeling assumptions and mathematical derivation. In Section 5, we verify analytical results through FE simulations, with respect to structural deformation measures (curvature, mid-axis strain, and the displacements of the cathode and the anode with respect to the mid-axis) and refined analysis in the vicinity of the electrodes of the counterions' concentration, electric potential, and strain fields. In Section 6, we conclude the paper with a discussion about the implications of our findings and an outlook on lines of future research.

2. Review of continuum model

Here, we briefly review the modeling framework proposed in Cha & Porfiri (2014). The framework is grounded in a thermodynamically-consistent continuum formulation, which allows for describing the mechanics and electrochemistry of an ionomer undergoing finite deformations. The model assumes that the ionomer consists of a negatively charged hyperelastic membrane, such that mechanical deformation of the ionomer will cause changes in the configuration of the fixed charges, distributed on the ionomer backbone. The ionomer is neutralized by counterions, which can move in the ionomer due to diffusion and electromigration. The reorganization of charges will ultimately lead to osmotic and electrostatic forces on the ionomer.

A Lagrangian approach is used to describe the motion of the ionomer. The reference configuration is stress-free, with the counterions balancing the anions anchored to the ionomer and zero electric field (Figure 1). The motion of the ionomer in time is described by the mapping

$$\mathbf{x} = \mathrm{x}(\mathbf{X}, t), \tag{1}$$

where $\mathbf{X}$ is a material point ant t is the time variable. The deformation gradient is

$$\mathbf{F}(\mathbf{X}, t) = \boldsymbol{\nabla}\mathrm{x}(\mathbf{X}, t), \tag{2}$$

where $\boldsymbol{\nabla}(\cdot)$ is the material gradient.

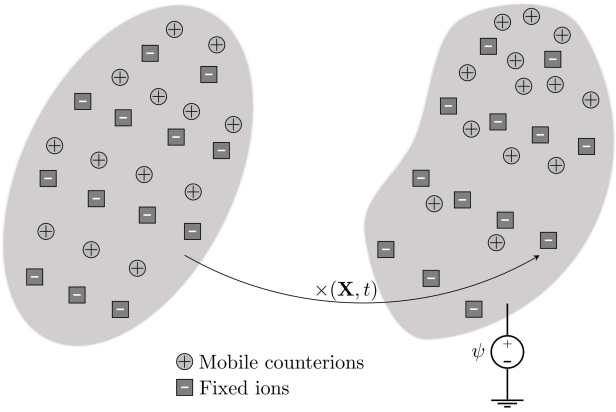

Figure 1: Illustration of the concurrent mechanical deformation and electrochemistry of the ionomer. The reference and the deformed configurations are shown on the left and right, respectively. In the deformed configuration, the migration of the mobile counterions upon the application of a voltage is displayed.

Assuming quasi-static deformations and neglecting body forces, the mechanical equilibrium is

$$\mathrm{Div}\ \mathbf{s} = 0, \tag{3}$$

where $\mathrm{Div}(\cdot)$ is the material divergence and $\mathbf{s}$ is the first Piola-Kirchhoff stress tensor. In general $\mathbf{s}$ is not a symmetric tensor, so that $\mathbf{s}\mathbf{F}^{\mathrm{T}} = \mathbf{F}\mathbf{s}^{\mathrm{T}}$ is required to satisfy the equilibrium of moments in a non-polar continuum (Gurtin et al., 2013), where T indicates tensor transposition.

The electrochemistry is described by the concentration of counterions per unit undeformed volume, C, and by the voltage, ψ, with respect to a common ground. From the electric potential, one can compute the nominal electric field $\tilde{\mathbf{E}} = -\boldsymbol{\nabla}\psi$. The mass conservation of the mobile counterions reads

$$\frac{\partial C}{\partial t} + \mathrm{Div}\ \mathbf{J} = 0, \tag{4}$$

where $\mathbf{J}$ is the counterions' flux.

Gauss law in the material configuration imposes

$$\text{Div}\ \tilde{\mathbf{D}} = Q, \tag{5}$$

where $\tilde{\mathbf{D}}$ is the nominal electric displacement and Q is the net charge per unit undeformed volume, which is equal to

$$Q = \mathcal{F}(C - C_0). \tag{6}$$

Here, $\mathcal{F} = 96485$ C mol^{-1} is the Faraday constant and C_0 is the fixed, constant, ion concentration per unit undeformed volume.

The constitutive equations for the ionomer are derived from the free-energy density, which we hypothesize to be composed of three contributions, namely,

$$W(\mathbf{F}, C, \tilde{\mathbf{D}}) = W_{\text{mec}}(\mathbf{F}) + W_{\text{ion}}(\mathbf{F}, C) + W_{\text{pol}}(\mathbf{F}, \tilde{\mathbf{D}}), \tag{7}$$

where $W_{\text{mec}}(\mathbf{F})$ is the elastic energy, $W_{\text{ion}}(\mathbf{F}, C)$ is the energy associated with the mixing of counterions and fixed ions, and $W_{\text{pol}}(\mathbf{F}, \tilde{\mathbf{D}})$ is the energy related to the polarization of the material.

Different modeling choices can be pursued to describe each of the energy contributions in Eq. (7). As a first approximation, we assume that the mechanical response follows a Saint-Venant-Kirchhoff model, such that

$$W_{\text{mec}}(\mathbf{F}) = \frac{\lambda_{\text{L}}}{2}(\text{tr}(\mathbf{L}))^2 + \mu_{\text{L}}\text{tr}(\mathbf{L})^2. \tag{8}$$

Here, $\mathbf{L} = \frac{1}{2}(\mathbf{F}^{\text{T}}\mathbf{F} - \mathbf{I})$ is the Green-Lagrange strain tensor, $\text{tr}(\cdot)$ is the trace, and λ_{L} and μ_{L} are the Lamé parameters. In what follows, we will often opt for the Poisson ratio, ν, and Young modulus, E, which are related to the Lamé parameters through (Timoshenko & Goodier, 2001)

$$\lambda_{\text{L}} = \frac{E\nu}{(1+\nu)(1-2\nu)}, \tag{9a}$$

$$\mu_{\text{L}} = \frac{E}{2(1+\nu)}. \tag{9b}$$

The energy contribution due to ion mixing is

$$W_{\text{ion}}(\mathbf{F}, C) = \mathcal{R}\mathcal{T}\left[C\left(\ln\frac{C}{C_0\det\mathbf{F}} - 1\right) - C_0\left(\ln\frac{1}{\det\mathbf{F}} - 1\right)\right], \tag{10}$$

where $\mathcal{R} = 8.314$ J mol^{-1} K^{-1} is the universal gas constant, $\mathcal{T}$ the absolute temperature, and $\det(\cdot)$ is the determinant. Finally, the contribution due to polarization reads

$$W_{\text{pol}}(\mathbf{F}, \tilde{\mathbf{D}}) = \frac{1}{2\epsilon}\frac{\mathbf{F}^{\text{T}}\mathbf{F}\cdot\tilde{\mathbf{D}}\otimes\tilde{\mathbf{D}}}{\det\mathbf{F}}, \tag{11}$$

where ϵ is the dielectric permittivity of the ionomer, "$\cdot$" is the inner product, and "$\otimes$" is the tensor product.

By differentiating the free-energy density with respect to the deformation gradient $\mathbf{F}$, we determine the first Piola-Kirchhoff stress tensor

$$\mathbf{s} = \mathbf{s}_{\mathrm{mec}} + \mathbf{s}_{\mathrm{ion}} + \mathbf{s}_{\mathrm{pol}}, \tag{12}$$

where

$$\mathbf{s}_{\mathrm{mec}} = \frac{\partial W_{\mathrm{mec}}}{\partial \mathbf{F}} = \mathbf{F}[\lambda_{\mathrm{L}} \mathrm{tr}(\mathbf{L})\mathbf{I} + 2\mu_{\mathrm{L}}\mathbf{L}], \tag{13a}$$

$$\mathbf{s}_{\mathrm{ion}} = \frac{\partial W_{\mathrm{ion}}}{\partial \mathbf{F}} = -\mathcal{R}\mathcal{T}(C - C_0)\mathbf{F}^{-\mathrm{T}}, \tag{13b}$$

$$\mathbf{s}_{\mathrm{pol}} = \frac{\partial W_{\mathrm{pol}}}{\partial \mathbf{F}} = \frac{1}{2\epsilon}\left(-\frac{\mathbf{F}^{\mathrm{T}}\mathbf{F}\cdot(\tilde{\mathbf{D}}\otimes\tilde{\mathbf{D}})\mathbf{F}^{-\mathrm{T}}}{\det\mathbf{F}} + \frac{2\mathbf{F}(\tilde{\mathbf{D}}\otimes\tilde{\mathbf{D}})}{\det\mathbf{F}}\right). \tag{13c}$$

Here, $\mathbf{s}_{\mathrm{mec}}$ is the stress associated with the hyperelastic behavior of the ionomer, $\mathbf{s}_{\mathrm{ion}}$ is the osmotic pressure, and $\mathbf{s}_{\mathrm{pol}}$ is the Maxwell stress.

With respect to the electrochemistry, the free-energy density yields the following constitutive relations for the nominal electric field and electrochemical potential μ:

$$\tilde{\mathbf{E}} = \frac{\partial W}{\partial \tilde{\mathbf{D}}} = \frac{1}{\epsilon \det\mathbf{F}}\mathbf{F}^{\mathrm{T}}\mathbf{F}\tilde{\mathbf{D}}, \tag{14a}$$

$$\mu = \mathcal{F}\psi + \frac{\partial W}{\partial C} = \mathcal{F}\psi + \mathcal{R}\mathcal{T}\ln\frac{C}{C_0 \det\mathbf{F}}. \tag{14b}$$

Finally, to ensure that the free-energy density does not increase, the constitutive behavior of the ion flux must obey

$$\mathbf{J}\cdot\boldsymbol{\nabla}\mu \leq 0, \tag{15}$$

which we satisfy by using the Lagrangian version of the classical Nernst-Planck equation (Bard & Faulkner, 2001) by setting

$$\mathbf{J} = -\frac{\mathcal{D}C}{\mathcal{R}\mathcal{T}}\mathbf{F}^{-1}\mathbf{F}^{-\mathrm{T}}\boldsymbol{\nabla}\mu, \tag{16}$$

where $\mathcal{D}$ is the counterions' diffusivity in the ionomer.

While it may be feasible to actuate an ionomer without electric contact as shown in Kim et al. (2016), ionomeric membranes are typically actuated through metal electrodes, formed on the ionomer via electroless plating (Oguro, Retrieved on August 10, 2018) or through direct assembly (Akle et al., 2007). The resulting composite material is what we call IPMC or, sometimes, ionic polymer transducer, see, for example, Akle et al. (2007, 2011). Different models have been proposed for the electrodes, spanning leaky conductors (Shahinpoor & Kim, 2002; Shen et al., 2015), composite layers with electrochemical properties (Cha et al., 2012), high-surface elecrodes with dispersed metal inclusions (Akle et al., 2011), and metal layers where redox reactions may take place (Johanson et al., 2015).

Here, we consider the simplest modeling choice, whereby the electrodes are considered to be perfect conductors that are impermeable to counterions' motion and have negligible mechanical properties. Therefore, on the portion of the ionomer that is plated by a metal electrode we set the following boundary conditions:

$$\mathbf{J} \cdot \mathbf{N} = 0, \tag{17a}$$

$$\psi = \bar{V}, \tag{17b}$$

where $\mathbf{N}$ is the outward normal to the ionomer in the reference configuration and $\bar{V}$ is the voltage at the electrode. Since the electrode is a perfect conductor, the applied voltage must be constant on the electrode. When studying actuation, this value is a priori chosen, while for sensing it will depend on the imposed mechanical deformation. On the portions of the ionomer that are not plated by the electrodes, different electrochemical boundary conditions may be contemplated, depending on the specific application one is interested in. For example, if the IPMC is in air or immersed in deionized water, one may impose that the normal component of the electric displacement is zero along with Eq. (17a) to prevent counterions to leave the ionomer.

Before concluding the section, a few remarks should be made. First, the hyperelastic response of the ionomer could be changed in favor of more complex models. The proposed FE solution can be easily adjusted accordingly, although the relatively small values of the deformations of ionomers in practical applications may not warrant the endeavor. In fact, in their typical use as actuators, IPMCs undergo macroscopic mechanical deformation of less than 5% (Akle & Leo, 2008), for which different hyperelastic models may produce comparable results (Batra, 2001). However, it is of value to formulate the problem from a more general finite deformations viewpoint, since displacements experienced by current IPMCs are often dramatically large and the availability of a general theory allows for better tackling potentially large deformations associated with electrochemical boundary layers, as we will demonstrate in this work. Similar to Porfiri et al. (2017), the model for ion mixing does not account for steric effects (Kilic et al., 2007a,b), which can be easily included by following the approach in Cha & Porfiri (2014). Here, we have opted for a simpler presentation of the framework to avoid confounding effects when examining the through-the-thickness deformations. Finally, we have assumed that all the physical quantities are spatially constant, although one may extend the approach to ionomers with graded properties. The latter may be particularly intriguing as additive manufacturing of IPMCs becomes more popular and there is a need to design and model three-dimensionally printed IPMCs.

3. Finite element formulation

Here, we pursue a numerical implementation of the nonlinear fully coupled equations of motion through the FE method. First, a weak formulation of the governing equations is obtained. A standard Galerkin

approach is adopted to project the equations on the FE set of basis functions. Finally, the FE equations are implemented in the commercial FE software Abaqus™ through a UEL, following examples available in the literature (Giner et al., 2009; Park & Paulino, 2012) and specializing to two-dimensional plane-strain. FE simulations, based on the nonlinear fully coupled model, are utilized as a benchmark to assess the validity of the exact solution proposed in the next Section.

3.1. Weak formulation

We indicate the entire undeformed domain with Ω and its boundary with $S = \partial\Omega$. For each equation, we identify two complementary subsets of the boundary, S_{D} and S_{N}, on which Dirichlet and Neumann boundary conditions are imposed, respectively. These subsets should satisfy the conditions $S_{\mathrm{D}} \cup S_{\mathrm{N}} = S$ and $S_{\mathrm{D}} \cap S_{\mathrm{N}} = \emptyset$. For Eqs. (3), (4), and (5), the following boundary conditions are considered, respectively:

$$\begin{cases} \mathbf{u} = \bar{\mathbf{u}} & \text{on } S_{\mathrm{D}_{\mathbf{u}}} \\ \mathbf{sN} = \mathbf{s}_{\mathrm{N}} & \text{on } S_{\mathrm{N}_{\mathbf{u}}} \end{cases}, \tag{18a}$$

$$\begin{cases} C = \bar{C} & \text{on } S_{\mathrm{D}_C} \\ \mathbf{J} \cdot \mathbf{N} = J_{\mathrm{N}} & \text{on } S_{\mathrm{N}_C} \end{cases}, \tag{18b}$$

$$\begin{cases} \psi = \bar{\psi} & \text{on } S_{\mathrm{D}_\psi} \\ \tilde{\mathbf{D}} \cdot \mathbf{N} = \tilde{D}_{\mathrm{N}} & \text{on } S_{\mathrm{N}_\psi} \end{cases}. \tag{18c}$$

With respect to the initial conditions, we assume that the initial configuration corresponds to the reference configuration, such that the displacement and potential are both zero, and that the concentration of mobile counterions and fixed ions are equal pointwise, that is,

$$\mathbf{u}(\mathbf{X}, 0) = 0, \tag{19a}$$

$$C(\mathbf{X}, 0) = C_0, \tag{19b}$$

$$\psi(\mathbf{X}, 0) = 0. \tag{19c}$$

A weak formulation of the governing equations in Eqs. (3), (4), and (5) is obtained by multiplying them with the corresponding variations, integrating over the entire domain Ω, and applying Gauss theorem to the divergence terms stemming from integration by parts. The test functions $\mathbf{w}_{\mathbf{u}}$, w_C, and w_ψ for the displacement field, counterions' concentration, and electric potential, respectively, are equal to zero over the

corresponding part of the boundary on which Dirichlet boundary conditions are imposed, that is, $S_{\mathrm{D}_\mathbf{u}}$, S_{D_C}, and S_{D_ψ}. The weak formulation of the equations thus reads

$$\int_{S_{\mathrm{N}_\mathbf{u}}} \mathbf{w_u} \cdot \mathbf{s}_\mathrm{N} \,\mathrm{d}S - \int_\Omega \boldsymbol{\nabla}\mathbf{w} \cdot \mathbf{s} \,\mathrm{d}\Omega = 0, \tag{20a}$$

$$\int_\Omega w_C \frac{\partial C}{\partial t} \,\mathrm{d}\Omega + \int_{S_{\mathrm{N}_C}} w_C J_\mathrm{N} \,\mathrm{d}S - \int_\Omega \boldsymbol{\nabla} w_C \cdot \mathbf{J} \,\mathrm{d}\Omega = 0, \tag{20b}$$

$$\int_{S_{\mathrm{N}_\psi}} w_\psi \tilde{D}_\mathrm{N} \,\mathrm{d}S_\mathrm{N} - \int_\Omega \boldsymbol{\nabla} w_\psi \cdot \tilde{\mathbf{D}} \,\mathrm{d}\Omega = \int_\Omega w_\psi \mathcal{F}(C - C_0) \,\mathrm{d}\Omega, \tag{20c}$$

where the first Piola-Kirchhoff stress tensor, the counterions' flux, and the electric displacement are related to displacement, counterions' concentration, and electric potential, through the constitutive equations in Eqs. (12), (16), and (14).

We now draw several hypotheses on the boundary conditions in order to simplify our problem, motivated by typical configurations of slender IPMC actuators (Jo et al., 2013; Shahinpoor, 2015). Regarding mechanical equilibrium, we assume that the boundary is stress-free where displacement is not imposed ($\mathbf{s}_\mathrm{N} = 0$ on $S_{\mathrm{N}_\mathbf{u}}$). This hypothesis could be relaxed in the implementation stage through the use of an auxiliary set of elements, superimposed to the user-defined elements for visualization of the results. Through standard Abaqus™ commands, one can apply external loads on default elements. To ensure that these fictitious elements have no influence on the response of the IPMC, we would impose that they have negligible stiffness compared to the user-defined elements. With respect to the mass conservation of counterions, we hypothesize that there is no flux of counterions anywhere on the boundary, that is, $J_\mathrm{N} = 0$, such that $S_{\mathrm{D}_C} = \emptyset$ and $S_{\mathrm{N}_C} = S$. This hypothesis is expected to be valid for applications in deionized water or air, where counterions would unlikely diffuse toward the surrounding environment even when electrodes are absent. Finally, with respect to Gauss law, we assume that S_{D_ψ} corresponds to the portion of the boundary where electrodes are plated, and we assume that the rest of the boundary has null normal component of the dielectric displacement. Similar to the case of counterions' flux, this condition should be valid for deionized water and air, where free charges cannot accumulate close to the ionomer surface. Under these assumptions, all the boundary terms in Eqs. (20a), (20b), and (20c) vanish.

A FE approximation is used to solve this problem numerically. The domain is partitioned into a set of distinct elements ($V = \bigcup V_e$) with N_nodes nodes in total. We suppose that the displacement field, counterions' concentration, and electric potential can be approximated as

$$\mathbf{u}(\mathbf{X}, t) \approx \sum_{k=1}^{N_\mathrm{nodes}} \phi^k(\mathbf{X}) \mathbf{u}^k(t), \tag{21a}$$

$$C(\mathbf{X}, t) \approx \sum_{k=1}^{N_\mathrm{nodes}} \phi^k(\mathbf{X}) C^k(t), \tag{21b}$$

$$\psi(\mathbf{X},t) \approx \sum_{k=1}^{N_{\text{nodes}}} \phi^k(\mathbf{X})\psi^k(t), \tag{21c}$$

where $\phi^k(\mathbf{X})$ is the FE basis function for the k-th node, and $\mathbf{u}^k(t)$, $C^k(t)$, and $\psi^k(t)$ are the nodal displacement, counterions' concentration, and potential, with $k = 1, \ldots, N_{\text{nodes}}$. Here, we choose the same set of basis functions for the all the scalar fields of the problem, but one may opt for using different elements for different fields.

We adopt a standard Galerkin approach, in which the test functions are approximated with the same basis functions of the unknown fields

$$\mathbf{w}_{\mathbf{u}}(\mathbf{X}) = \sum_k \phi^k(\mathbf{X})\mathbf{w}_{\mathbf{u}}^k, \tag{22a}$$

$$w_C(\mathbf{X}) = \sum_k \phi^k(\mathbf{X})w_C^k, \tag{22b}$$

$$w_\psi(\mathbf{X}) = \sum_k \phi^k(\mathbf{X})w_\psi^k. \tag{22c}$$

Upon substitution of these projections in the weak formulation in Eq. (20) and accounting for the arbitrariness of the nodal variations $\mathbf{w}_{\mathbf{u}}^k$, w_C^k, and w_ψ^k, the following equations are obtained:

$$\int_\Omega \mathbf{s} \cdot \boldsymbol{\nabla}\phi^k \,\mathrm{d}\Omega = 0, \tag{23a}$$

$$\int_\Omega \phi^k \frac{\partial C}{\partial t} \,\mathrm{d}\Omega - \int_\Omega \boldsymbol{\nabla}\phi^k \cdot \mathbf{J} \,\mathrm{d}\Omega = 0, \tag{23b}$$

$$-\int_\Omega \boldsymbol{\nabla}\phi^k \cdot \tilde{\mathbf{D}} \,\mathrm{d}\Omega = \int_\Omega \phi^k \mathcal{F}(C - C_0) \,\mathrm{d}\Omega. \tag{23c}$$

Here, the first Piola-Kirchhoff stress tensor, counterions' flux, and electric displacement are all related to the nodal variables through the constitutive equations in Eqs. (12), (16), and (14), with the displacement, concentration, and potential given by the FE approximation in Eq. (21).

Given that the FE basis functions have a compact support in each element, integrals in Eq. (23) shall be evaluated at the element level. More specifically, for a generic element Ω_{el}, we should solve the following equations:

$$\int_{\Omega_{\text{el}}} \mathbf{s} \cdot \boldsymbol{\nabla} N^i \,\mathrm{d}\Omega = 0, \tag{24a}$$

$$\int_{\Omega_{\text{el}}} N^i \frac{\partial C}{\partial t} \,\mathrm{d}\Omega - \int_{\Omega_{\text{el}}} \boldsymbol{\nabla} N^i \cdot \mathbf{J} \,\mathrm{d}\Omega = 0, \tag{24b}$$

$$-\int_{\Omega_{\mathrm{el}}} \boldsymbol{\nabla} N^i \cdot \tilde{\mathbf{D}}\, \mathrm{d}\Omega = \int_{\Omega_{\mathrm{el}}} N^i \mathcal{F}(C - C_0)\, \mathrm{d}\Omega, \tag{24c}$$

where $N^i(\mathbf{X})$ are shape functions on Ω_{el}, with $i = 1, \ldots, N_{\mathrm{nodes_{el}}}$, with $N_{\mathrm{nodes_{el}}}$ being the total number of nodes per element. These equations correspond to the sought FE formulation at the element level, upon replacing for the stress, counterions' flux, and dielectric displacement the constitutive equations in Eqs. (12), (16), and (14) with the displacement, concentration, and potential given by the approximation in Eq. (21).

3.2. Implementation in Abaqus™

The FE equations in Eq. (24) are first nondimensionalized as in Cha & Porfiri (2014) and then implemented through a UEL in the commercial FE software Abaqus™, following the example in Chester et al. (2015). Abaqus™ employs an implicit Newton solver to compute the solution of the problem in time. The solver requires the computation of the residuals and the tangents (that is, the Jacobians) in the UEL subroutine from the tentative values of the nodal displacements, counterions' concentrations, and electric potentials at the following time step. The nodal residuals are

$$\mathbf{R}^i_{\mathbf{u}} = \int_{\Omega_{\mathrm{el}}} \mathbf{s} \cdot \boldsymbol{\nabla} N^i\, \mathrm{d}\Omega, \tag{25a}$$

$$R^i_C = \int_{\Omega_{\mathrm{el}}} N^i \frac{\partial C}{\partial t}\, \mathrm{d}\Omega - \int_{\Omega_{\mathrm{el}}} \boldsymbol{\nabla} N^i \cdot \mathbf{J}\, \mathrm{d}\Omega, \tag{25b}$$

$$R^i_\psi = \int_{\Omega_{\mathrm{el}}} \boldsymbol{\nabla} N^i \cdot \tilde{\mathbf{D}}\, \mathrm{d}\Omega + \int_{\Omega_{\mathrm{el}}} N^i \mathcal{F}(C - C_0)\, \mathrm{d}\Omega. \tag{25c}$$

The tangents are computed as

$$\mathbf{K}^{ij}_{\mathbf{uu}} = -\frac{\partial \mathbf{R}^i_{\mathbf{u}}}{\partial \mathbf{u}^j}, \tag{26a}$$

$$\mathbf{K}^{ij}_{\mathbf{u}C} = -\frac{\partial \mathbf{R}^i_{\mathbf{u}}}{\partial C^j}, \tag{26b}$$

$$\mathbf{K}^{ij}_{\mathbf{u}\psi} = -\frac{\partial \mathbf{R}^i_{\mathbf{u}}}{\partial \psi^j}, \tag{26c}$$

$$\mathbf{K}^{ij}_{C\mathbf{u}} = -\frac{\partial R^i_C}{\partial \mathbf{u}^j}, \tag{26d}$$

$$K^{ij}_{CC} = -\frac{\partial R^i_C}{\partial C^j}, \tag{26e}$$

$$K^{ij}_{C\psi} = -\frac{\partial R^i_C}{\partial \psi^j}, \tag{26f}$$

$$\mathbf{K}^{ij}_{\psi\mathbf{u}} = -\frac{\partial R^i_\psi}{\partial \mathbf{u}^j}, \tag{26g}$$

$$K^{ij}_{\psi C} = -\frac{\partial R^i_\psi}{\partial C^j}, \tag{26h}$$

$$K^{ij}_{\psi\psi} = -\frac{\partial R^i_\psi}{\partial \psi^j}. \tag{26i}$$

The expressions of these matrices are presented in Appendix A.

The integrals in the residuals and in the tangents are computed numerically through standard Gauss integration, upon mapping the physical element into a standard domain; since this is a common practice in FE codes, we do not include here the details, but we refer to FE literature, see, for example, Belytschko et al. (2014). The constitutive equations in Eqs. (12), (16), and (14) and their derivatives are used to compute the quantities contained in the integrals at each integration point.

Although this procedure is identical in one, two, or three dimensions, we focus on a two-dimensional plane-strain problem, whereby we seek to examine the coupling between axial and through-the-thickness deformations, under the premise that gradients of the variables along the width of the IPMC are negligible. In order to quantify nonlinear effects in the mechanical response of the ionomer, we retain the full coupling between electrochemistry and mechanics and we study finite deformations. For this reason, an eight nodes quadratic plane-strain element has been implemented (Figure 3.2). Plane-strain conditions are imposed by setting $F_{ZZ} = 1$ and $F_{XZ} = F_{YZ} = F_{ZX} = F_{ZY} = 0$ in the user subroutine. For this element, nine Gauss integration points are required for full integration (Lapidus & Pinder, 2011).

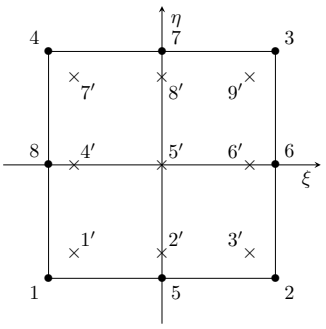

Figure 2: Sketch of the implemented eight node two-dimensional element. Dots indicate the nodes, while crosses are used for the Gauss integration points. Their numbering is also shown.

The use of a quadratic element has a two-fold purpose. In addition to higher accuracy with respect to linear elements, quadratic elements are more robust to volumetric locking, which is often observed in simulations of nearly incompressible solids with low-order finite elements (Zienkiewicz & Taylor, 2013). Several solutions have been proposed in the literature to overcome this problem, based on reduced integration

(Fried, 1974) and modification of the deformation gradient (de Souza Neto et al., 1996). Reduced integration is simple to implement, but its solution may contain hourglass modes, that is, non-physical zero-energy modes, which require stabilization (Reese & Wriggers, 2000). On the other hand, techniques involving a modification of the deformation gradient might significantly complicate the implementation of the element, especially in the case of fully coupled multiphysics problems. The use of a quadratic element considerably mitigates the effect of volumetric locking, although not completely suppressing it.

4. Analytical solution for uniform bending

The modeling framework in Section 2 constitutes the starting point for examining actuation and sensing of IPMCs. Here, we seek to establish an analytical solution to IPMC actuation in two-dimensions, extending previous research that has only focused on beam-like structural models. Toward this goal, we first introduce two key simplifications for the continuum model, and then turn to the analytical solution for the actuation of a slender IPMC. The study of IPMC actuation is divided into two steps. First, we study the through-the-thickness electrochemistry building on prior work (Porfiri, 2008), and then we extend the analysis to the study of mechanical deformation.

4.1. Problem setting

Despite the large deflections documented in the literature, experimental results indicate that axial strains usually do not exceed 5% (Akle & Leo, 2008), thereby supporting the possibility of using linear theories to study IPMC mechanics. Hence, we hypothesize that the ionomer undergoes small deformations, such that the present configuration can be assimilated to the reference configuration. This hypothesis is systematically examined in Section 5, where we compare the predictions of the analytical solution based on linear elasticity with nonlinear FE simulations.

Within classical, linear elasticity, the first Piola-Kirchhoff stress tensor can be assimilated to the, symmetric, Cauchy stress tensor (Gurtin et al., 2013). We retain only leading order terms in the constitutive equations for the stress, such that neither the contributions from ion mixing and polarization contain explicit dependence on the mechanical deformation. Therefore, the three contributions from mechanical deformation, ion mixing, and dielectric polarization become

$$\mathbf{s}_{\mathrm{mec}} = \lambda_{\mathrm{L}} \mathrm{tr}(\boldsymbol{\varepsilon})\mathbf{I} + 2\mu_{\mathrm{L}}\boldsymbol{\varepsilon}, \tag{27a}$$

$$\mathbf{s}_{\mathrm{ion}} = -\mathcal{R}\mathcal{T}(C - C_0)\mathbf{I}, \tag{27b}$$

$$\mathbf{s}_{\mathrm{pol}} = \frac{1}{2\epsilon}\left[-\mathrm{tr}(\tilde{\mathbf{D}} \otimes \tilde{\mathbf{D}})\mathbf{I} + 2\tilde{\mathbf{D}} \otimes \tilde{\mathbf{D}}\right], \tag{27c}$$

where $\boldsymbol{\varepsilon} = \text{sym}\,\mathbf{H}$ is the small deformations strain tensor, $\text{sym}(\cdot)$ is the symmetric part of a tensor, and $\mathbf{H} = \mathbf{F} - \mathbf{I}$ is the displacement gradient.

The second key hypothesis for our analytical treatment is that the effect of mechanical deformation on the IPMC electrochemistry is negligible. Thus, we turn to the electrochemistry, so that Eqs. (14) and (16) become

$$\tilde{\mathbf{E}} = \frac{1}{\epsilon}\tilde{\mathbf{D}}, \tag{28a}$$

$$\mu = \mathcal{F}\psi + \mathcal{R}\mathcal{T}\ln\frac{C}{C_0}, \tag{28b}$$

$$\mathbf{J} = -\frac{\mathcal{D}C}{\mathcal{R}\mathcal{T}}\boldsymbol{\nabla}\mu. \tag{28c}$$

Within this modeling framework, the electrochemistry taking place within the ionomer is entirely decoupled from the mechanical deformation, and it can be solved once for all. Upon solving the electrochemistry, one can compute the Maxwell stress and the osmotic pressure, and ultimately calculate the deformation of the IPMC. This approach shares similarities with classical linear thermoelastic problems, in which one would determine first the temperature profile in a material and then compute the associated thermal stress, ultimately used to predict the mechanical deformation (Thornton, 1996). Different from linear thermoelastic problems, the solution of the electrochemistry problem is highly nonlinear. With respect to IPMC actuation and beam-like models, the validity of these approximations has been discussed in Porfiri et al. (2017) and Porfiri et al. (2018). Theoretical and numerical results presented therein suggest that, for small deformations, the effect of the ionomer deformation on the electrochemistry is secondary — the complete FE analysis presented in Section 5 will reinforce these claims in a more general plane-strain two-dimensional setting with finite deformations.

Under these premises, we examine a thin strip of ionomer of length L and thickness $2h \ll L$, undergoing plane-strain deformation (Figure 3). We consider a reference frame with the X-coordinate along the IPMC mid-axis and the Y-coordinate axis along the thickness direction. The Z-coordinate runs through the depth of the IPMC. The ionomer is plated on the top and bottom surfaces, which are kept at the voltage $\frac{\bar{V}}{2}$ and $-\frac{\bar{V}}{2}$, respectively. On the lateral surfaces we assume that the electric displacement in the X-direction is zero, which can be an adequate approximation for operation in air of deionized water, as explained in Section 3. Consistent with Section 3, on the same surfaces, we set the normal component of the counterions' flux to zero to prevent counterions' transport in the environment, which, again, should be valid for air and deionized water. All the surfaces of the IPMC are assumed to be stress-free. We block the displacement of the origin and the axial displacement of the point on the mid-axis at $X = L$.

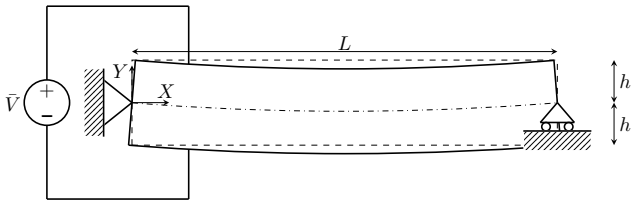

Figure 3: Schematics of the problem. Solid lines represent the deformed condition, while dashed lines are the initial undeformed configuration. The dashed-dotted line is the deformed mid-axis.

4.2. Electrochemistry

Away from the lateral surfaces, we can neglect the axial components of the counterions' flux and the electric field, such that both the electric potential and the counterions' concentration will only depend on Y and t. Therefore, Eqs. (28a), (28b), and (28c) lead to the following one-dimensional Poisson-Nernst-Planck (PNP) system of equations to be solved for C and ψ:

$$-\epsilon\frac{\partial^2\psi(Y,t)}{\partial Y^2} = \mathcal{F}(C(Y,t) - C_0), \tag{29a}$$

$$\frac{\partial C(Y,t)}{\partial t} = \mathcal{D}\left[\frac{\partial^2 C(Y,t)}{\partial Y^2} + \frac{\mathcal{F}}{\mathcal{RT}}\frac{\partial}{\partial Y}\left(C(Y,t)\frac{\partial\psi(Y,t)}{\partial Y}\right)\right]. \tag{29b}$$

Boundary conditions for the problem are

$$J(\pm h,t) = -\mathcal{D}\left(\frac{\partial C(\pm h,t)}{\partial Y} + \frac{\mathcal{F}C(\pm h,t)}{\mathcal{RT}}\frac{\partial\psi(\pm h,t)}{\partial Y}\right) = 0, \qquad t > 0, \tag{30a}$$

$$\psi(\pm h,t) = \pm\frac{\bar{V}(t)}{2}, \qquad t > 0, \tag{30b}$$

while the initial conditions are

$$C(Y,0) = C_0, \tag{31a}$$

$$\psi(Y,0) = \frac{\bar{V}(0)}{2}\frac{Y}{h}. \tag{31b}$$

We note that the charge per unit surface stored on the electrodes, q_{S}, is computed from the value of the electric displacement on either of the electrodes, such that

$$q_{\mathrm{S}}(t) = \epsilon\frac{\partial\psi(h,t)}{\partial Y} = \epsilon\frac{\partial\psi(-h,t)}{\partial Y}. \tag{32}$$

This set of nonlinear partial differential equations corresponds to a singularly perturbed problem, which can be solved analytically by using the method of matched asymptotic expansions. Details of the solution are presented in Porfiri (2008). Briefly, the method consists of the subdivision of the domain in three regions: two "inner" subdomains near the electrodes, in which a magnified variable is used to represent the

formation of the boundary layers, and an "outer" subdomain in the bulk of the ionomer. The solution is expanded, both for the inner and outer regions, into a power series of $\delta = \frac{1}{\mathcal{F}h}\sqrt{\frac{\epsilon\mathcal{R}\mathcal{T}}{C_0}} \ll 1$, which is the ratio between the Debye screening length and the ionomer thickness. The unknown functional coefficients of the power series for both regions can be determined sequentially by solving simpler problems in the inner and outer regions, using boundary conditions and matching conditions between the overlapping inner and outer subdomains. A composite solution valid on the entire domain is finally recovered by combining the inner and outer solutions.

From the asymptotic solution, it is possible to formulate an elegant physically-based circuit model for the IPMC, which illuminates the key phenomena taking place during actuation (Figure 4). The circuit is composed of a voltage source, associated with the voltage applied across the electrodes, and an impedance, quantifying the IPMC response. The impedance is constituted by a nonlinear capacitor and a linear resistor. The capacitor encapsulates the formation of electric double layers during the counterions' pile-up and depletion toward the cathode and anode, respectively.

The constitutive behavior of the capacitor is

$$q_{\mathrm{S}}(t) = \sqrt{\epsilon\mathcal{R}\mathcal{T}C_0}\,\vartheta\left(\frac{V(t)}{V_{\mathrm{th}}}\right), \tag{33}$$

where $V_{\mathrm{th}} = \frac{\mathcal{R}\mathcal{T}}{\mathcal{F}}$ is the so-called thermal voltage, and

$$\vartheta(\alpha) = \sqrt{2}\sqrt{\frac{\alpha}{\exp(\alpha)-1} - \ln\frac{\alpha}{\exp(\alpha)-1} - 1}, \tag{34}$$

where $\alpha = \frac{V}{V_{\mathrm{th}}}$ is the nondimensional voltage across the terminals of the capacitor. The resistor, instead, is associated with the counterions' motion through the ionomer. The conductivity is given by

$$\sigma = \frac{\mathcal{D}C_0\mathcal{F}^2}{2h\mathcal{R}\mathcal{T}}. \tag{35}$$

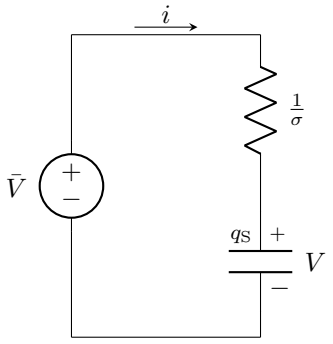

Figure 4: Schematics of the physically-based circuit model for an IPMC, adapted from Porfiri (2008). Note that all the variables refer to an IPMC of unit surface, such that for an IPMC of area A, the resistance will be $\frac{1}{A\sigma}$, the charge stored Aq_{s}, and the current Ai.

From Kirchhoff's law, we have

$$\bar{V}(t) = V(t) + \frac{i(t)}{\sigma}, \tag{36}$$

where $i(t) = \frac{\mathrm{d}q_{\mathrm{S}}(t)}{\mathrm{d}t}$ is the current per unit IPMC surface. To study the time response of the IPMC, we integrate Eq. (36) with respect to $V(t)$ with initial condition $V(0) = 0$, due to the fact that at time $t = 0$, the ionomer is electroneutral. From $V(t)$, we can compute the electrochemistry throughout the ionomer as follows:

$$C(Y, \alpha(t)) = C_0 \left[-1 + \exp\left(y^+ \left(\frac{1 - \frac{Y}{h}}{\delta}, \alpha(t) \right) \right) + \exp\left(y^- \left(\frac{1 + \frac{Y}{h}}{\delta}, \alpha(t) \right) \right) \right], \tag{37a}$$

$$\psi(Y, \alpha(t)) = \frac{\bar{V}(t)}{2} + \frac{i(t)}{2\sigma} \left(\frac{Y}{h} - 1 \right) + V_{\mathrm{th}} \left[\ln\left(\frac{\alpha(t)}{\exp(\alpha(t)) - 1} \right) - y^+ \left(\frac{1 - \frac{Y}{h}}{\delta}, \alpha(t) \right) - y^- \left(\frac{1 + \frac{Y}{h}}{\delta}, \alpha(t) \right) \right]. \tag{37b}$$

Here, the two functions $y^{\pm}(\xi^{\pm}, \alpha(t))$ are given as the solutions of the Cauchy problems

$$\frac{\partial^2 y^{\pm}(\xi^{\pm}, \alpha)}{(\partial \xi^{\pm})^2} = \exp(y^{\pm}(\xi^{\pm}, \alpha)) - 1, \tag{38a}$$

$$y^+(0, \alpha) = \ln \frac{\alpha}{\exp(\alpha) - 1}, \tag{38b}$$

$$y^-(0, \alpha) = \ln \frac{\alpha}{\exp(\alpha) - 1} + \alpha, \tag{38c}$$

$$\frac{\partial y^{\pm}(0, \alpha)}{\partial \xi^{\pm}} = \pm \vartheta(\alpha), \tag{38d}$$

in which $\xi^{\pm} = \frac{1 \mp \frac{Y}{h}}{\delta}$ are magnifying nondimensional variables near the electrodes.

Each of the nonlinear ordinary differential equations in Eq. (38a) can be solved a-priori as a function of α. Thus, the problem of the spatial and temporal evolutions for the IPMC electrochemistry are completely decoupled. From the analysis of the circuit, we compute $V(t)$ and $i(t)$, and from Eq. (37) we obtain the profile of the concentration and electric potential. The solution of the PNP problem for C and ψ was the objective of Porfiri (2008), where the ionomer was assumed to be mechanically rigid. Here, we extend the study to the computation of the mechanical deformation in an exact form. Achieving this goal requires several technical advancements to the matched asymptotic expansion solution, as detailed below.

4.3. Mechanical deformation

From the solution of the PNP problem, we evaluate both the contributions to the stress from ion mixing and dielectric polarization in Eqs. (13b) and (13c), which away from the lateral surfaces of the IPMC are

$$s_{\mathrm{ion}_{XX}}(Y, t) = s_{\mathrm{ion}_{YY}}(Y, t) = s_{\mathrm{ion}_{ZZ}}(Y, t) = -\mathcal{R}\mathcal{T}(C(Y, t) - C_0), \tag{39a}$$

$$s_{\mathrm{ion}_{XY}} = s_{\mathrm{ion}_{XZ}} = s_{\mathrm{ion}_{YX}} = s_{\mathrm{ion}_{ZX}} = 0, \tag{39b}$$

$$s_{\mathrm{pol}_{XX}}(Y,t) = s_{\mathrm{pol}_{ZZ}}(Y,t) = -\frac{\epsilon}{2}\left(\frac{\partial\psi}{\partial Y}(Y,t)\right)^2, \tag{39c}$$

$$s_{\mathrm{pol}_{YY}}(Y,t) = \frac{\epsilon}{2}\left(\frac{\partial\psi}{\partial Y}(Y,t)\right)^2, \tag{39d}$$

$$s_{\mathrm{pol}_{XY}} = s_{\mathrm{pol}_{XZ}} = s_{\mathrm{pol}_{YX}} = s_{\mathrm{pol}_{ZX}} = 0. \tag{39e}$$

Both the osmotic pressure and the Maxwell stress are independent of the axial coordinate and do not include shear contributions. From the solution of the PNP problem, all these terms can be explicitly written in terms of the voltage across the capacitor and the current through it. In what follows, we demonstrate closed-forms for their resultants, which can be used for inferring salient measures of the deformation of the IPMC.

Following the classical Saint-Venant approach to linear elasticity, away from the two lateral surfaces we search for a solution of the problem in the form of uniform bending. Toward this aim, we hypothesize a compatible strain field (Timoshenko & Goodier, 2001) as follows. We assume that the axial component of the strain is given by

$$\varepsilon_{XX}(Y,t) = -k(t)Y + \varepsilon_0(t), \tag{40}$$

where $k(t)$ is the constant curvature of the mid-axis and $\varepsilon_0(t)$ is the mid-axis strain. Similarly, we set the shear strain ε_{XY} to zero and we hypothesize that the through-the-thickness strain does not depend on the axial coordinate. The rich dependence of the through-the-thickness strain on Y is one of the key findings of this study. If $\mathrm{Curl}(\cdot)$ is the material curl of a vector, these conditions ensure that

$$\mathrm{Curl}(\mathrm{Curl}(\boldsymbol{\varepsilon})) = 0, \tag{41}$$

such that a plane-strain displacement field (Timoshenko & Goodier, 2001) can be reconstructed from integration, namely,

$$u_X(X,Y,t) = [-k(t)Y + \varepsilon_0(t)]X + A_X(Y,t), \tag{42a}$$

$$u_Y(X,Y,t) = \int_0^Y \varepsilon_{YY}(\hat{Y},t)\,\mathrm{d}\hat{Y} + A_Y(X,t), \tag{42b}$$

where the integration functions $A_X(Y,t)$ and $A_Y(X,t)$ are related by the following condition:

$$\frac{\partial A_X}{\partial Y}(Y,t) = k(t)X - \frac{\partial A_Y}{\partial X}(X,t), \tag{43}$$

which guarantees zero shear strain. Considering an IPMC of length L, simply supported as in Figure 3, these integration functions should verify that the displacement at the origin is zero and the component of the displacement along the Y-axis is zero at $X = L$ and $Y = 0$. Thus, in this case, we would find

$$u_X(X, Y, t) = [-k(t)Y + \varepsilon_0(t)]X + \frac{1}{2}kLY, \tag{44a}$$

$$u_Y(X, Y, t) = \int_0^Y \varepsilon_{YY}(\hat{Y}, t)\, \mathrm{d}\hat{Y} + \frac{1}{2}kX(X - L). \tag{44b}$$

Next, we evaluate the stress components from Eq. (12), which become

$$s_{XX} = (\lambda_\mathrm{L} + 2\mu_\mathrm{L})\varepsilon_{XX} + \lambda_\mathrm{L}\varepsilon_{YY} + s_{\mathrm{ion}_{XX}} + s_{\mathrm{pol}_{XX}}, \tag{45a}$$

$$s_{YY} = (\lambda_\mathrm{L} + 2\mu_\mathrm{L})\varepsilon_{YY} + \lambda_\mathrm{L}\varepsilon_{XX} + s_{\mathrm{ion}_{YY}} + s_{\mathrm{pol}_{YY}}, \tag{45b}$$

$$s_{ZZ} = \lambda_\mathrm{L}(\varepsilon_{XX} + \varepsilon_{YY}) + s_{\mathrm{ion}_{ZZ}} + s_{\mathrm{pol}_{ZZ}}, \tag{45c}$$

$$s_{XY} = s_{YX} = s_{XZ} = s_{ZX} = 0, \tag{45d}$$

where the components associated with Maxwell stress and osmotic pressure are given in Eq. (39). These components must satisfy the equilibrium equations, the boundary conditions on the top and bottom surfaces pointwise, and the boundary conditions on the lateral surface in terms of the force and moment resultants.

With respect to the equilibrium equations in Eq. (3), it is easy to verify that they are satisfied pointwise upon setting the through-the-thickness component of the stress to zero. The latter condition also guarantees that the boundary conditions on the top and bottom surfaces are satisfied. Thus, setting Eq. (45b) to zero and replacing for Eqs. (39a) and (39d), the through-the-thickness strain takes the following form:

$$\varepsilon_{YY} = -\frac{\lambda_\mathrm{L}}{\lambda_\mathrm{L} + 2\mu_\mathrm{L}}(-kY + \varepsilon_0) + \frac{1}{\lambda_\mathrm{L} + 2\mu_\mathrm{L}}\mathcal{R}\mathcal{T}(C - C_0) - \frac{1}{\lambda_\mathrm{L} + 2\mu_\mathrm{L}}\frac{\epsilon}{2}\left(\frac{\partial\psi}{\partial Y}\right)^2. \tag{46}$$

In sharp contrast with the axial strain in Eq. (40), Eq. (46) implies a complex spatial variation of the through-the-thickness strain, controlled by the formation of the electric double layers in the vicinity of the electrodes. Both the variations of the counterions' concentration and the electric potential from Eq. (37) contribute to strain localization toward the electrodes.

Notably, from Eq. (46), we can compute the change in thickness experienced by the IPMC during actuation as

$$\Delta(t) = \int_{-h}^{h} \varepsilon_{YY}(\hat{Y}, t)\, \mathrm{d}\hat{Y}. \tag{47}$$

Specifically, by replacing Eq. (46) in Eq. (47) and considering the counterion-blocking condition in Eq. (30a) (ensuring that the integral of the charge density over the thickness is always zero), we determine

$$\Delta(t) = -2h\frac{\lambda_{\mathrm{L}}}{\lambda_{\mathrm{L}}+2\mu_{\mathrm{L}}}\varepsilon_0(t) - \frac{1}{\lambda_{\mathrm{L}}+2\mu_{\mathrm{L}}}\frac{\epsilon}{2}\int_{-h}^{h}\left(\frac{\partial\psi}{\partial\hat{Y}}(\hat{Y},t)\right)^2 \mathrm{d}\hat{Y}. \tag{48}$$

The anode and cathode regions contribute differentially to the macroscopic thickness contraction in Eq. (48), since the through-the-thickness strain ε_{YY} is in general not symmetric with respect to the mid-axis. It is thus convenient to decompose the contraction Δ into the sum of two contributions, associated with the cathode and anode, that is,

$$\Delta_-(t) = \int_{-h}^{0}\varepsilon_{YY}(\hat{Y},t)\,\mathrm{d}\hat{Y}, \tag{49a}$$

$$\Delta_+(t) = \int_{0}^{h}\varepsilon_{YY}(\hat{Y},t)\,\mathrm{d}\hat{Y}. \tag{49b}$$

These quantities represent the change in thickness of the lower and upper halves of the IPMC, respectively.

To calculate the curvature and axial strain at the mid-axis, we compute the stress resultants from the axial component of the stress

$$N(t) = \int_{-h}^{h} s_{XX}(\hat{Y},t)\,\mathrm{d}\hat{Y}, \tag{50a}$$

$$M(t) = -\int_{-h}^{h} s_{XX}(\hat{Y},t)\hat{Y}\,\mathrm{d}\hat{Y}. \tag{50b}$$

We start the analysis by enforcing equilibrium on the force resultant to compute the axial deformation ε_0 Eq. (40), and then we turn to the moment resultant to calculate the curvature k in Eq. (40).

By setting the force resultant in (50a) to zero and using Eqs. (39a), (39c), and (45a), the axial deformation is computed as

$$\varepsilon_0(t) = \frac{\epsilon}{8\mu_{\mathrm{L}}h}\int_{-h}^{h}\left(\frac{\partial\psi}{\partial\hat{Y}}(\hat{Y},t)\right)^2 \mathrm{d}\hat{Y}. \tag{51}$$

This expression can be further simplified by integrating by parts, using Eq. (32) that ensures that the electric field is the same close to the two electrodes, and Poisson equation in Eq. (29), so that

$$\varepsilon_0(t) = \frac{1}{4\mu_{\mathrm{L}}h}\left[\frac{q_{\mathrm{S}}^2(t)}{\epsilon}h + \mathcal{F}\int_{-h}^{h}(C(\hat{Y},t)-C_0)\frac{\partial\psi}{\partial\hat{Y}}(\hat{Y},t)\hat{Y}\,\mathrm{d}\hat{Y}\right]. \tag{52}$$

Similarly, by imposing that the moment resultant in Eq. (50b) is zero and using Eqs. (45a), (39a), and (39c), we determine the following equation for the curvature of the IPMC:

$$\beta k(t) + M_{\mathrm{ion}}(t) + M_{\mathrm{pol}}(t) = 0, \tag{53}$$

where the bending stiffness of the IPMC and the contributions of the moment associated with ion mixing and dielectric polarization are given by

$$\beta = \frac{8}{3}\mu_{\mathrm{L}}\frac{\lambda_{\mathrm{L}}+\mu_{\mathrm{L}}}{\lambda_{\mathrm{L}}+2\mu_{\mathrm{L}}}h^3, \tag{54a}$$

$$M_{\rm ion}(t) = 2\frac{\mu_{\rm L}}{\lambda_{\rm L}+2\mu_{\rm L}}\mathcal{R}\mathcal{T}\int_{-h}^{h}(C(\hat{Y},t)-C_0)\hat{Y}\,\mathrm{d}\hat{Y}, \tag{54b}$$

$$M_{\rm pol}(t) = \frac{\lambda_{\rm L}+\mu_{\rm L}}{\lambda_{\rm L}+2\mu_{\rm L}}\epsilon\int_{-h}^{h}\left(\frac{\partial\psi}{\partial\hat{Y}}(\hat{Y},t)\right)^2\hat{Y}\,\mathrm{d}\hat{Y}. \tag{54c}$$

Both Eqs. (54b) and (54c) can be simplified by using the PNP equations in Eq. (37). More specifically, by carrying out the integration by parts in $M_{\rm ion}$, using Poisson equation in Eq. (29), the definition of the charge per unit surface in Eq. (32), and the boundary condition for the electric potential across the electrodes in Eq. (30b), we determine

$$M_{\rm ion}(t) = 2\frac{\mu_{\rm L}}{\lambda_{\rm L}+2\mu_{\rm L}}\frac{\mathcal{R}\mathcal{T}}{\mathcal{F}}\left[\epsilon\bar{V}(t)-2q_{\rm S}(t)h\right]. \tag{55}$$

Analogously, with respect to $M_{\rm pol}$, we carry out an integration by parts and use again the fact that the electric field is the same close to the electrodes, see Eq. (32), to find

$$M_{\rm pol}(t) = \frac{\lambda_{\rm L}+\mu_{\rm L}}{\lambda_{\rm L}+2\mu_{\rm L}}\mathcal{F}\int_{-h}^{h}(C(\hat{Y},t)-C_0)\frac{\partial\psi}{\partial\hat{Y}}(\hat{Y},t)\frac{\hat{Y}^2}{2}\,\mathrm{d}\hat{Y}. \tag{56}$$

By using Eq. (34) and recalling that $\delta \ll 1$, the expression for $M_{\rm ion}$ can be approximated as

$$M_{\rm ion}(t) = -4M_0\frac{\mu_{\rm L}}{\lambda_{\rm L}+2\mu_{\rm L}}\delta\vartheta(\alpha(t)), \tag{57}$$

where $M_0 = \mathcal{R}\mathcal{T}C_0h^2$. We remark that the contribution of the osmotic pressure to the bending moment in Eq. (57) depends only on the voltage across the electric double layers of the IPMC.

The expression for $M_{\rm pol}$ requires more effort. Upon nondimensionalization of the integral in Eq. (56), we obtain

$$M_{\rm pol}(t) = \frac{\lambda_{\rm L}+\mu_{\rm L}}{\lambda_{\rm L}+2\mu_{\rm L}}M_0\int_{-1}^{1}(\tilde{C}(\tilde{Y},t)-1)\frac{\partial\tilde{\psi}}{\partial\tilde{Y}}(\tilde{Y},t)\tilde{Y}^2\,\mathrm{d}\tilde{Y}, \tag{58}$$

where we have used the dimensionless variables $\tilde{Y} = \frac{Y}{h}$, $\tilde{C} = \frac{C}{C_0}$, and $\tilde{\psi} = \frac{\psi}{V_{\rm th}}$. The contribution from the bulk to this integral is negligible, since outside the boundary layers $\tilde{C} \approx 1$. Upon discarding the effect of the bulk, substituting the boundary layers' terms from Eq. (37), and recalling that $\delta \ll 1$, the integral reads

$$\begin{aligned}\int_{-1}^{1}(\tilde{C}(\tilde{Y},t)-1)\frac{\partial\tilde{\psi}}{\partial\tilde{Y}}(\tilde{Y},t)\tilde{Y}^2\,\mathrm{d}\tilde{Y} &= \\ = \int_0^\infty(e^{y^+(\alpha(t),\xi^+)}-1)\frac{\partial y^+}{\partial\xi^+}(\alpha(t),\xi^+)\,\mathrm{d}\xi^+ &- \int_0^\infty(e^{y^-(\alpha(t),\xi^-)}-1)\frac{\partial y^-}{\partial\xi^-}(\alpha(t),\xi^-)\,\mathrm{d}\xi^- + 2\delta\mathcal{G}(\alpha),\end{aligned} \tag{59}$$

where we have introduced

$$\mathcal{G}(\alpha) = \int_0^\infty(e^{y^-}-1)\frac{\partial y^-}{\partial\xi^-}\xi^-\,\mathrm{d}\xi^- - \int_0^\infty(e^{y^+}-1)\frac{\partial y^+}{\partial\xi^+}\xi^+\,\mathrm{d}\xi^+. \tag{60}$$

Here and in what follows, we omit some functional dependencies in the asymptotic expansions for improved legibility. Substituting Eqs. (38a) and (38d), and using the relations $\lim_{\xi^\pm\to\infty}y^\pm(\xi^\pm,\alpha) = 0$ (Porfiri, 2008),

we find

$$\int_0^\infty (e^{y^\pm}-1)\frac{\partial y^\pm}{\partial \xi^\pm}\,\mathrm{d}\xi^\pm = \left[\frac{1}{2}(y^\pm(\xi^\pm,\alpha))^2\right]_0^\infty = -\frac{1}{2}(y^\pm(0,\alpha))^2 = -\frac{1}{2}\vartheta^2(\alpha), \tag{61}$$

so that

$$\int_0^\infty (e^{y^+}-1)\frac{\partial y^+}{\partial \xi^+}\,\mathrm{d}\xi^+ - \int_0^\infty (e^{y^-}-1)\frac{\partial y^-}{\partial \xi^-}\,\mathrm{d}\xi^- = 0. \tag{62}$$

Therefore, by substituting the remaining term from Eq. (59) in Eq. (58), the bending moment associated with the polarization reduces to

$$M_{\mathrm{pol}}(t) = 2M_0\frac{\lambda_\mathrm{L}+\mu_\mathrm{L}}{\lambda_\mathrm{L}+2\mu_\mathrm{L}}\delta\mathcal{G}(\alpha(t)). \tag{63}$$

Equivalent expressions for ε_0 and Δ can be obtained. First, we note that these two quantities can be related by substituting Eq. (51) into Eq. (48), so that

$$\Delta(t) = -2h\varepsilon_0(t). \tag{64}$$

Equation (64) indicates that, irrespective of material properties, the mid-axis strain should equal in magnitude the average through-the-thickness strain, see Eq. (47), such that the area occupied by the IPMC is the same throughout the entire deformation. Using Eq. (33) into Eq.(52) and nondimensionalizing the integral, we obtain

$$\varepsilon_0(t) = \frac{\mathcal{R}\mathcal{T}C_0}{4\mu_\mathrm{L}}\left[\vartheta^2(\alpha(t)) + \int_{-1}^1 (\tilde{C}(\tilde{Y},t)-1)\frac{\partial\tilde{\psi}}{\partial\tilde{Y}}(\tilde{Y},t)\tilde{Y}\,\mathrm{d}\tilde{Y}\right]. \tag{65}$$

Again, we comment that the the contribution to the integral from the bulk is negligible. Substituting the boundary layers' terms from Eqs. (37) into Eq. (65) and employing Eq. (61), the following expression is obtained:

$$\int_{-1}^1 (\tilde{C}(\tilde{Y},t)-1)\frac{\partial\tilde{\psi}}{\partial\tilde{Y}}(\tilde{Y},t)\tilde{Y}\,\mathrm{d}\tilde{Y} = -\vartheta^2(\alpha(t)) + \frac{1}{2}\delta\mathcal{H}(\alpha(t)), \tag{66}$$

where

$$\mathcal{H}(\alpha) = -2\left[\int_0^\infty (e^{y^-}-1)\frac{\partial y^-}{\partial\xi^-}\xi^-\,\mathrm{d}\xi^- + \int_0^\infty (e^{y^+}-1)\frac{\partial y^+}{\partial\xi^+}\xi^+\,\mathrm{d}\xi^+\right]. \tag{67}$$

Substituting Eq. (66) in Eq. (65) finally leads to

$$\varepsilon_0(t) = \frac{\mathcal{R}\mathcal{T}C_0}{8\mu_\mathrm{L}}\delta\mathcal{H}(\alpha(t)). \tag{68}$$

Similarly, from Eq. (64), the thickness contraction is obtained as

$$\Delta(t) = -\frac{\mathcal{R}\mathcal{T}C_0 h}{4\mu_\mathrm{L}}\delta\mathcal{H}(\alpha(t)). \tag{69}$$

The displacements of the cathode and the anode can be obtained in a similar way. Substituting Eq. (46) into Eq. (49) and performing the integration of the first summand in each expression, we find

$$\begin{aligned}\Delta_-(t) = &-\frac{\lambda_\mathrm{L}}{\lambda_\mathrm{L}+2\mu_\mathrm{L}}\left(-k(t)\frac{h^2}{2}+\varepsilon_0(t)h\right)+\\ &+\frac{1}{\lambda_\mathrm{L}+2\mu_\mathrm{L}}\mathcal{R}\mathcal{T}\int_{-h}^0 (C(\hat{Y},t)-C_0)\,\mathrm{d}\hat{Y} - \frac{1}{\lambda_\mathrm{L}+2\mu_\mathrm{L}}\frac{\epsilon}{2}\int_{-h}^0\left(\frac{\partial\psi}{\partial\hat{Y}}\right)^2(\hat{Y},t)\,\mathrm{d}\hat{Y},\end{aligned} \tag{70a}$$

$$\Delta_+(t) = -\frac{\lambda_\mathrm{L}}{\lambda_\mathrm{L}+2\mu_\mathrm{L}}\left(k(t)\frac{h^2}{2}+\varepsilon_0(t)h\right)+ \\ +\frac{1}{\lambda_\mathrm{L}+2\mu_\mathrm{L}}\mathcal{RT}\int_0^h (C(\hat{Y},t)-C_0)\,\mathrm{d}\hat{Y}-\frac{1}{\lambda_\mathrm{L}+2\mu_\mathrm{L}}\frac{\epsilon}{2}\int_0^h\left(\frac{\partial\psi}{\partial\hat{Y}}\right)^2(\hat{Y},t)\,\mathrm{d}\hat{Y}. \tag{70b}$$

The second integral in Eq. (70) can be solved from the PNP system in Eq. (29). Specifically, by integrating Poisson equation and using Eq. (32), we find

$$\int_{-h}^0 (C(\hat{Y},t)-C_0)\,\mathrm{d}\hat{Y} = -\int_0^h (C(\hat{Y},t)-C_0)\,\mathrm{d}\hat{Y}. \tag{71}$$

Next, we substitute the composite solution in Eq. (37) and neglect higher order terms in δ, corresponding to the contribution of the bulk, obtaining

$$\int_{-h}^0 (C(\hat{Y},t)-C_0)\,\mathrm{d}\hat{Y} = -\int_0^h (C(\hat{Y},t)-C_0)\,\mathrm{d}\hat{Y} = \delta C_0 h\vartheta(\alpha(t)). \tag{72}$$

The last integrals in Eq. (70) are analogous to those associated with $\varepsilon_0(t)$, see Eq. (51). Following the same steps for obtaining Eq. (68), we determine

$$\epsilon\int_{-h}^0\left(\frac{\partial\psi}{\partial\hat{Y}}\right)^2(\hat{Y},t)\,\mathrm{d}\hat{Y} = -2\mathcal{RT}C_0h\delta\int_0^\infty (e^{y^-}-1)\frac{\partial y^-}{\partial\xi^-}\xi^-\,\mathrm{d}\xi^-, \tag{73a}$$

$$\epsilon\int_0^h\left(\frac{\partial\psi}{\partial\hat{Y}}\right)^2(\hat{Y},t)\,\mathrm{d}\hat{Y} = -2\mathcal{RT}C_0h\delta\int_0^\infty (e^{y^+}-1)\frac{\partial y^+}{\partial\xi^+}\xi^+\,\mathrm{d}\xi^+. \tag{73b}$$

Recalling the definitions of $\mathcal{G}(\alpha)$ and $\mathcal{H}(\alpha)$ in Eqs. (60) and (67), we finally establish

$$\epsilon\int_{-h}^0\left(\frac{\partial\psi}{\partial\hat{Y}}\right)^2(\hat{Y},t)\,\mathrm{d}\hat{Y} = -\mathcal{RT}C_0h\delta\left(\mathcal{G}(\alpha(t))-\frac{\mathcal{H}(\alpha(t))}{2}\right), \tag{74a}$$

$$\epsilon\int_0^h\left(\frac{\partial\psi}{\partial\hat{Y}}\right)^2(\hat{Y},t)\,\mathrm{d}\hat{Y} = \mathcal{RT}C_0h\delta\left(\mathcal{G}(\alpha(t))+\frac{\mathcal{H}(\alpha(t))}{2}\right). \tag{74b}$$

Upon substituting Eqs. (72) and (74) into Eq. (70), and using (53), (54a), (57), (63), and (68), we establish

$$\Delta_-(t) = -\frac{1}{\lambda_\mathrm{L}+2\mu_\mathrm{L}}\mathcal{RT}C_0\delta h\left(-\frac{\lambda_\mathrm{L}+4\mu_\mathrm{L}}{4(\lambda_\mathrm{L}+\mu_\mathrm{L})}\vartheta(\alpha(t))-\frac{3\lambda_\mathrm{L}+4\mu_\mathrm{L}}{8\mu_\mathrm{L}}\mathcal{G}(\alpha(t))+\frac{\lambda_\mathrm{L}+2\mu_\mathrm{L}}{8\mu_\mathrm{L}}\mathcal{H}(\alpha(t))\right), \tag{75a}$$

$$\Delta_+(t) = -\frac{1}{\lambda_\mathrm{L}+2\mu_\mathrm{L}}\mathcal{RT}C_0\delta h\left(\frac{\lambda_\mathrm{L}+4\mu_\mathrm{L}}{4(\lambda_\mathrm{L}+\mu_\mathrm{L})}\vartheta(\alpha(t))+\frac{3\lambda_\mathrm{L}+4\mu_\mathrm{L}}{8\mu_\mathrm{L}}\mathcal{G}(\alpha(t))+\frac{\lambda_\mathrm{L}+2\mu_\mathrm{L}}{8\mu_\mathrm{L}}\mathcal{H}(\alpha(t))\right). \tag{75b}$$

We remark that the sum of the two equations in Eq. (75) is equivalent to Eq. (64), as expected.

We note that $\vartheta(\alpha)$, $\mathcal{G}(\alpha)$, and $\mathcal{H}(\alpha)$ depend only on the dimensionless voltage across the electric double layers, and they are valid for every IPMC, since they do not vary with material properties. While $\vartheta(\alpha)$ is

explicitly available from Eq. (34), $\mathcal{G}(\alpha)$ and $\mathcal{H}(\alpha)$ have to be computed by integrating numerically their expression in Eqs. (60) and (67). These last two functions are plotted in Figure 5a. Given that $M_{\text{ion}}(t)$, $M_{\text{pol}}(t)$, $\varepsilon_0(t)$, $\Delta_-(t)$, and $\Delta_+(t)$ depend on time only through the functions $\vartheta(\alpha(t))$, $\mathcal{G}(\alpha(t))$, and $\mathcal{H}(\alpha(t))$, their time evolution can be obtained by solving first for $\alpha(t)$ the equivalent circuit from Eq. (36) and then substituting this function in their expression.

Due to the fact that $\vartheta(\alpha)$, $\mathcal{G}(\alpha)$, and $\mathcal{H}(\alpha)$ are positive for $\alpha > 0$, from Eqs. (57), (63), (68), and (69) we obtain that M_{pol} and ε_0 are always positive, while M_{ion}, Δ, and Δ_+ are negative. In other words, during its actuation, the IPMC is subjected to an elongation in the axial direction and a reduction of the thickness, which become more severe with larger applied voltage. The sign of Δ_- can change in time as a function of the applied voltage and the material parameters, although its absolute value, when positive, must be less than $|\Delta_+|$.

The curvature of the IPMC is determined by the interplay between the positive moment due to polarization and the negative moment related to the osmotic pressure, as dictated by Eq. (53). To understand the relative importance of these contributions, we compute the ratio of their absolute values from Eqs. (63) and (57), and substitute the definition of the Lamé parameters from Eq. (9),

$$\left|\frac{M_{\text{pol}}(t)}{M_{\text{ion}}(t)}\right| = \frac{1}{1-2\nu}\frac{\mathcal{G}(\alpha(t))}{2\mathcal{H}(\alpha(t))}. \tag{76}$$

This ratio as a function of α is shown in Figure 5b for different values of the Poisson ratio. The horizontal dashed line identifies where the moment due to polarization is larger (above the line) from where the ionic contribution prevails (below the line). As expected, Maxwell stress becomes more important as the internal voltage α increases, while the osmotic pressure dominates at lower voltages.

Due to their difference in sign, osmotic pressure induces a curvature toward the anode, while Maxwell stress generates a curvature toward the cathode. As originally proposed in Porfiri et al. (2017), the nonlinear interplay between these two terms, compactly illustrated in Figure 5b, may be the physical reason underpinning the phenomenon of back-relaxation. Discovered more than twenty years ago by Asaka et al. (1995), this effect consists of an initial bending of the IPMC toward the anode, followed by a slow relaxation toward the cathode for a fixed imposed step voltage (Porfiri et al., 2017, 2018). According to our model, a step voltage generates an increasing, nondimensional, voltage $\alpha(t)$ across the capacitor (Figure 4), whose time evolution predicts the occurrence of back-relaxation. Initially, α is small and the osmotic pressure dominates IPMC actuation, causing a deflection toward the anode. As time increases, the voltage across the double layers approaches the input voltage. If this voltage is sufficiently large, Maxwell stress can overcome osmotic pressure, thereby inducing back-relaxation toward the cathode. The minimum value of the input voltage for which back-relaxation can occur is given by the intersection of the plotted curve with the horizontal dashed line. The existence of a cross over value for the input voltage that leads to back-relaxation has been partially documented in Del Bufalo et al. (2008).

Through the analysis of two-dimensional deformation, we demonstrate for the first time that the interaction between osmotic pressure and Maxwell stress is modulated by the Poisson ratio. We demonstrate that the cross over value depends nonlinearly on the Poisson ratio. The sensitivity of the dependence increases as the ionomer approaches the incompressibility limit of $\nu = 0.5$. In this limit condition, the osmotic pressure seems to have a negligible effect on the deformation, due to its spherical nature. Therefore, no initial deformation toward the anode should occur, and Maxwell stress should elicit bending toward the cathode for any value of the input voltage. This complex behavior would not be captured by using standard beam theory (Porfiri et al., 2017, 2018), which would predict the case of $\nu = 0$.

Analogous considerations can be put forward for the displacements of the cathode and the anode with respect to the mid-axis. We already observed that Δ_+ and $\Delta = \Delta_+ + \Delta_-$ are negative. For this reason, Δ_-, when positive, must be less in magnitude than Δ_+ to ensure an overall thickness contraction. Toward investigating the relative importance of these contributions on the thickness contraction, we compute the ratio between Δ_- and Δ_+ from Eq. (75)

$$\frac{\Delta_-(t)}{\Delta_+(t)} = \frac{-2(1-2\nu)(2-3\nu)\vartheta(\alpha(t)) - (2-\nu)\mathcal{G}(\alpha(t)) + (1-\nu)\mathcal{H}(\alpha(t))}{2(1-2\nu)(2-3\nu)\vartheta(\alpha(t)) + (2-\nu)\mathcal{G}(\alpha(t)) + (1-\nu)\mathcal{H}(\alpha(t))}, \tag{77}$$

where we have substituted the definition of the Lamé parameters from Eq. (9). This ratio as a function of α for different values of the Poisson ratio is shown in Figure 5c. For all the values of the Poisson ratio, the curve approaches -1 as the voltage tends to zero, guaranteeing null contraction without an applied voltage. In addition, the curve is always less than one in absolute value for all the values of voltage and Poisson ratio. The contraction of the upper half of the IPMC is therefore always higher than the deformation of the lower half, ensuring that the overall thickness is reduced.

An applied voltage causes an increase of the distance between the mid-axis and the cathode, but this effect becomes secondary with respect to the contraction of the upper half of the IPMC for high voltages. More specifically, for any value of ν, the curve approaches a horizontal asymptote below zero. Toward the incompressible limit, we observe a peak in the curve for small values of the applied voltage, indicating that both the cathodic and anodic regions experience a contraction. In this case, the factors multiplying $\vartheta(\alpha)$ tend to zero, such that the contribution associated with the osmotic pressure vanishes. This observation confirms our claim that the Poisson ratio has a fundamental role in shaping the interplay between osmotic pressure and Maxwell stress, whereby the former becomes secondary as the Poisson ratio increases.

5. Results

This section is organized as follows. First, we describe the methodology used to compute both the FE and exact solutions. Second, we examine global structural measures for different values of the applied voltage and different Poisson ratios, comparing the FE and exact solutions. Therein, we specifically examine the bending

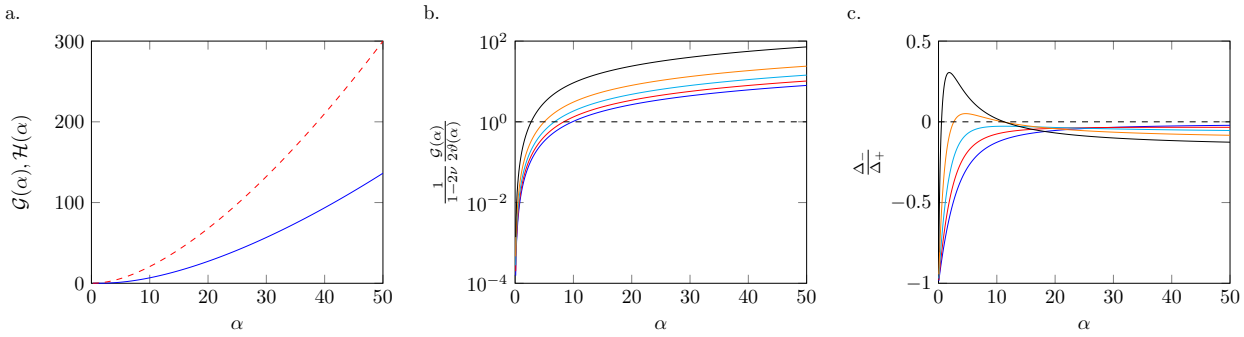

Figure 5: a. Plot of the two functions $\mathcal{G}$ (solid blue line) and $\mathcal{H}$ (red dashed line). b. Absolute value of the ratio of the bending moments due to osmotic pressure and Maxwell stress by varying the Poisson ratio. From right to left, the Poisson ratio of each curve is 0.05 (blue), 0.15 (red), 0.25 (cyan), 0.35 (orange), and 0.45 (black). The dashed line corresponds to the cross over condition $M_{\text{ion}} = -M_{\text{pol}}$. c. Ratio of the displacements of the cathode and anode by varying the Poisson ratio. The Poisson ratio of each curve is 0.05 (blue), 0.15 (red), 0.25 (cyan), 0.35 (orange), and 0.45 (black). The dashed line corresponds to $\Delta_- = 0$.

curvature, the mid-axis strain, and the displacement of the electrodes with respect to the mid-axis. For the most severe case of actuation, we study the profiles of the counterions' concentration, electric potential, and strain through the thickness of the IPMC. All the analysis is carried out using the material and geometric properties listed in Table 1, representing a typical Nafion-based IPMC from prior work in Porfiri et al. (2017), for a step input voltage of value $\bar{V}$. For this choice of the ionomer parameters, $\delta = 1 \times 10^{-3}$.

Parameter	Value
$\mathcal{T}$ [K]	300
C_0 [mol m^{-3}]	1200
$\mathcal{D}$ [m^2 s^{-1}]	1×10^{-11}
h [μm]	100
ϵ [F m^{-1}]	4.48×10^{-5}
E [GPa]	0.15

Table 1: Model parameters used in the simulations.

The FE solution is computed on a slender rectangular domain with $L = 20h$. The mesh consists of 32,000 elements, which correspond to a characteristic length of $0.025h$, with a refinement of twenty elements near each electrode, whose characteristic length is $0.0005h$. As in Figure 3, we block the displacement at the origin and we set to zero the vertical displacement of the mid-axis at $X = L$. Another mesh of fictitious

built-in Abaqus™ elements with negligible mechanical and electrical properties is superimposed for data visualization, along with evaluation of the deformation. To foster convergence, the step input is replaced with a steep ramp, which linearly increases until 10^{-3} s. Automatic time stepping is used, with the solver being forced to compute the solution every 0.25 s. The typical computational time on a standard computer is around one hour. The outputs of the FE code are the nodal displacements, counterions' concentration, electric potential, and planar components of the nominal strain tensor at each time instant for which the solution is computed. The nominal strain tensor is defined as

$$\bar{\boldsymbol{\varepsilon}} = \sqrt{\mathbf{F}\mathbf{F}^{\mathrm{T}}} - \mathbf{I}. \tag{78}$$

To mitigate edge effects, we use the cross-section at the mid-span for computing all the salient quantities of the analysis. At each time step, the curvature and the mid-axis strain are estimated by using a linear regression on $\bar{\varepsilon}_{XX}$ in Matlab®, according to Eq. (40). The motion of the electrodes with respect to the mid-axis is obtained from the difference of the displacement along the Y-axis of the mid-axis and the top and bottom surfaces. The profiles for the counterions' concentration, electric potential, and planar components of the nominal strain tensor are directly available from the output of the FE simulation.

The exact solution is computed by integrating the first order nonlinear differential equation for the voltage across the capacitor in Eq. (36) in Mathematica, using the built-in function "NDSolve". From the time trace of V, we compute the bending moment M_{ion} due to osmotic pressure, the bending moment M_{pol} due to Maxwell stress, the curvature k, the mid-axis strain ε_0, and the displacements of the cathode Δ_- and anode Δ_+ with respect to the mid-axis using Eqs. (57), (63), (53), (68), and (75), respectively. For a given time $t^\star = 1$ s during the evolution, the profiles of the counterions' concentration C and voltage ψ are computed from the composite solution from Eq. (37), and the axial strain ε_{XX} and the through-the-thickness strain ε_{YY} from Eq. (40) and (46), respectively. The functions $y^{\pm}(\xi^{\pm}, \alpha)$ are obtained by integrating Eq. (38) with the function "NDSolve" with $\xi^{\pm}$ in a range from 0 to 20. The functions $\mathcal{G}(\alpha)$ and $\mathcal{H}(\alpha)$ shown in Figure 5a are computed by evaluating the integrals in Eqs. (60) and (67), respectively, with the built-in function "NIntegrate". For the range $0 < \alpha < 50$, the functions $\mathcal{G}$ and $\mathcal{H}$ in Eqs. (60) and (67), respectively, are well approximated by the following polynomial expressions:

$$\mathcal{G}(\alpha) \approx 7.24723 \times 10^{-6}\alpha^4 - 1.125 \times 10^{-3}\alpha^3 + 0.09624\alpha^2 - 0.1764\alpha, \tag{79a}$$

$$\mathcal{H}(\alpha) \approx -4.65973 \times 10^{-7}\alpha^5 + 7.42926 \times 10^{-5}\alpha^4 - 4.93736 \times 10^{-3}\alpha^3 + 0.236939\alpha^2 + 0.115022\alpha, \tag{79b}$$

which are obtained with 200 points for α in the interval $[0, 50]$. These expressions guarantee an error of less than 1% for $\alpha > 0.05$, that is, excluding the points in which the functions are approximately zero.

5.1. Structural deformation measures

In Figures 6 and 7, we display the time evolution of the curvature, mid-axis strain, and displacements of the electrodes with respect to the mid-axis for three different voltage levels ($\bar{\alpha} = 1$, 5, and 10) and Poisson ratio of 0.05 and 0.45, respectively. For small applied voltages, the analytical solution is in very good agreement with FE results, with respect to the curvature, mid-axis strain, and displacement of the electrodes for both values of the Poisson ratio. As the voltage increases, the analytical solution is successful in capturing the curvature and mid-axis strain for both values of the Poisson ratio, although modest discrepancies can be observed on the curvature at the largest voltage for $\nu = 0.05$. The underprediction of the curvature is due to the severity of the through-the-thickness deformation which cannot be captured by linear elasticity. As discussed in the following Subsection, for $\nu = 0.05$, we register a five-fold increase in the nominal through-the-thickness strain with respect to the case $\nu = 0.45$ for the largest applied voltage. Differences between analytical and FE results are amplified when examining the displacement of the anode, whereby the exact solution fails to quantitatively capture the steady-state displacement with respect to the mid-axis for the smallest value of the Poisson ratio at intermediate and high levels of the applied voltage.

Delving more into the comparison between the exact and FE solution, we register that for small applied voltages and $\nu = 0.05$, the displacement of the electrodes predicted by the exact solution is in excellent agreement with FE simulations. The analytical solution is able to capture the displacement of the cathode with respect to the mid-axis also for the intermediate and large values of voltage. However, a discrepancy for the steady-state displacement of the anode quickly arises as the voltage increases to intermediate and large values. Close to the incompressible limit, instead, the exact solution is in very good agreement with FE results for all the tested voltage levels. The reason for this Poisson ratio-dependent discrepancy should again be sought in the severity of the through-the-thickness deformations, which challenge the premise of the linear elastic solution, whereby we register near the anode a steady-state through-the-thickness strain of about 9% and 30% for the intermediate and high voltage levels, respectively. Within linear elasticity, we predict that the mid-axis strain should match the average through-the-thickness strain, irrespective of the Poisson ratio, but, considering finite deformations, this claim holds true only for nearly incompressible materials, which will be more conducive to deformations that preserve the overall area of the IPMC.

For both the selected values of Poisson ratio, low values of the applied voltage (Figures 6a and 7a) lead to the monotonic bending of the IPMC toward the cathode, without evidence of back-relaxation, in agreement with experimental evidence in Del Bufalo et al. (2008). Bending is accompanied by stretching along the mid-axis, which, however, happens at a slower time rate than bending (Figures 6d and 7d). Likely, this is due to the fact that stretching along the mid-axis is exclusively driven by Maxwell stress, as shown in Eq. (52), which, in turn, is dominated by osmotic effects with respect to bending. While Maxwell stress is quadratic in the electric potential, osmotic pressure is characterized by a linear dependence, thereby explaining the different time scales of evolution. An equivalent response is noted for the displacement of the anode with

respect to the mid-axis, which monotonically decreases with time toward a steady-state value (Figures 6j and 7j). Comparing the responses for the two selected values of Poisson ratio, we register a decrease in the severity of the deformation as we approach the incompressible limit. This is agreement with the discussion in Section 4.3 about the role of the Poisson ratio on the interplay between osmotic pressure and Maxwell stress.

As expected, the dependence of the displacement of the cathode on the Poisson ratio is more complex. For the lower value of the Poisson ratio, we register a monotonic expansion of the lower half of the IPMC (Figure 6g), which is less severe than the contraction of the upper half, producing an overall thickness contraction. The displacement of the cathode for $\nu = 0.45$, instead, presents an initial expansion followed by a contraction (Figure 7g). Similar to back-relaxation, this can be explained by the charging process of the internal capacitor in Figure 4 when a step voltage is applied. Initially, the voltage across the capacitor is small, leading to an initial expansion of the lower half of the IPMC (see Figure 5c). As the voltage across the capacitor increases and approaches the external voltage, the lower half of the IPMC contracts since the ratio between Δ_- and Δ_+ becomes positive. This phenomenon leads to an amplification of the thickness contraction in the incompressible limit, despite the fact that the contraction of the upper half is smaller.

At intermediate values of the applied voltage, we identify a significant difference between the structural response of the IPMC for the two selected values of the Poisson ratio. While a continuous bending toward the cathode is noted for the smaller value of the Poisson ratio, a remarkable back-relaxation is registered for the larger value of the Poisson ratio (Figures 6b and 7b). Surprisingly, bending is more severe for the smaller value of the Poisson ratio, of approximately one order of magnitude. This should be attributed to the fact that $\bar{\alpha} = 5$ is close to the cross over voltage for the nearly-incompressible limit in Figure 5b, such that at steady-state the contributions to the bending moment from Maxwell stress and osmotic pressure perfectly balance each other and the IPMC cannot bend. Should we use a beam-like approximation for the IPMC deformation as in Porfiri et al. (2017) and Porfiri et al. (2018), we would fail in accurately identifying the effect of the Poisson ratio. Specifically, we would conclude that there is not back-relaxation, irrespective of the value of the Poisson ratio, since our prediction would coincide with the ideal case of $\nu = 0$. The mid-axis strain and displacement of the anode with respect to the mid-axis at the intermediate value of the applied voltage are similar to those computed for small voltage, whereby we observe more robust mid-axis strain and less severe contraction of the upper half of the IPMC for the larger value of the Poisson ratio (Figures 6e, 6k, 7e, and 7k). With respect to the displacement of the cathode, we register an increase in the absolute value of the deformation for both the values of the Poisson ratio (Figure 6h and 7h). For $\nu = 0.45$, the time scale of the charge of the internal capacitor in Figure 4 is remarkably reduced, such that no significant initial expansion is observed. Finally, we comment that the time scale of back-relaxation in Figure 7b matches the time scale of the mid-axis strain and contraction of the thickness, thereby confirming the intuition that Maxwell stress is the driver for the slower dynamics for moderate values of the applied voltage.

Results on the curvature for the largest value of the applied voltage indicate a mild back-relaxation for the lower value of the Poisson ratio (Figure 6c) and a more severe back-relaxation for the larger one (Figure 7c). While for $\nu = 0.05$, back-relaxation brings the sample back to a curvature close to zero, a robust bending toward the cathode is observed for $\nu = 0.45$. In fact, for the larger value of the Poisson ratio, the initial bending toward the cathode is not appreciable, whereby the sample seems to bend continuously toward the anode. As expected, larger bending is attained close to the incompressible limit. The mid-axis strain reaches a relatively large value on the order of 0.01% for both values of the Poisson ratio, with more severe deformations attained for $\nu = 0.45$ (Figures 6f and 7f). The displacement of the anode displays equivalently large values (Figures 6l and 7l). For this voltage level, the analytical solution suggests more severe contraction of the upper half of the IPMC for the higher Poisson ratio, while FE predictions indicate the opposite due to the nonlinear deformation regime. Results on the displacement of the cathode for $\nu = 0.05$ are analogous to those for lower voltages, although exhibiting an expected increase due to the higher value of the applied voltage (Figure 6i). For the larger value of the Poisson ratio, we observe a contraction of the lower half of the IPMC that reaches a peak and finally decreases in magnitude. To explain this behavior, we consider again the charging process of the internal capacitor in Figure 4. In this case, the external voltage is higher than the voltage at which the maximum of the curve at $\nu = 0.45$ in Figure 5c is attained. For this reason, after the initial contraction observed for lower voltage levels, a mechanical relaxation of the deformation is observed.

Potentially, mid-axis strain at $\bar{\alpha} = 10$ could be experimentally reconstructed by using strain-gages on the electrodes of the IPMCs. For this voltage level, through-the-thickness deformation of the IPMC is also on the order of 0.01%, which might be measured using high-resolution imaging. However, empirical data to support this claim are presently not available and acquiring these data will be the object of future experimental research. Experiments should also be carried out to validate our predictions on the role of Poisson ratio, which might be controlled by varying the level of hydration of the sample or changing the ionomer material. Presently, most of the data on ionomers used as core materials for IPMCs indicate Poisson ratio between 0.2 and 0.487 (Silberstein & Boyce, 2010; Page et al., 2015; Li & Nemat-Nasser, 2000).

5.2. Counterions' concentration, electric potential, and strain through the thickness

The profiles of the counterions' concentration, electric potential, and planar components of the strain tensor at $t^\star = 1$ s for the largest applied voltage, that is, $\bar{\alpha} = 10$, are studied herein. Figures 8 and 9 display the profiles of the counterions' concentration and electric potential through the thickness for both the values of the Poisson ratio. In both cases, FE simulations agree very well with the analytical solution, while a small difference can be observed on the electric potential, mostly, for the smaller value of the Poisson ratio. In this case the exact solution underpredicts the value of the bulk voltage toward the anode. This is associated with the difference between the curvature values in Figure 6c, which we attribute to the severity

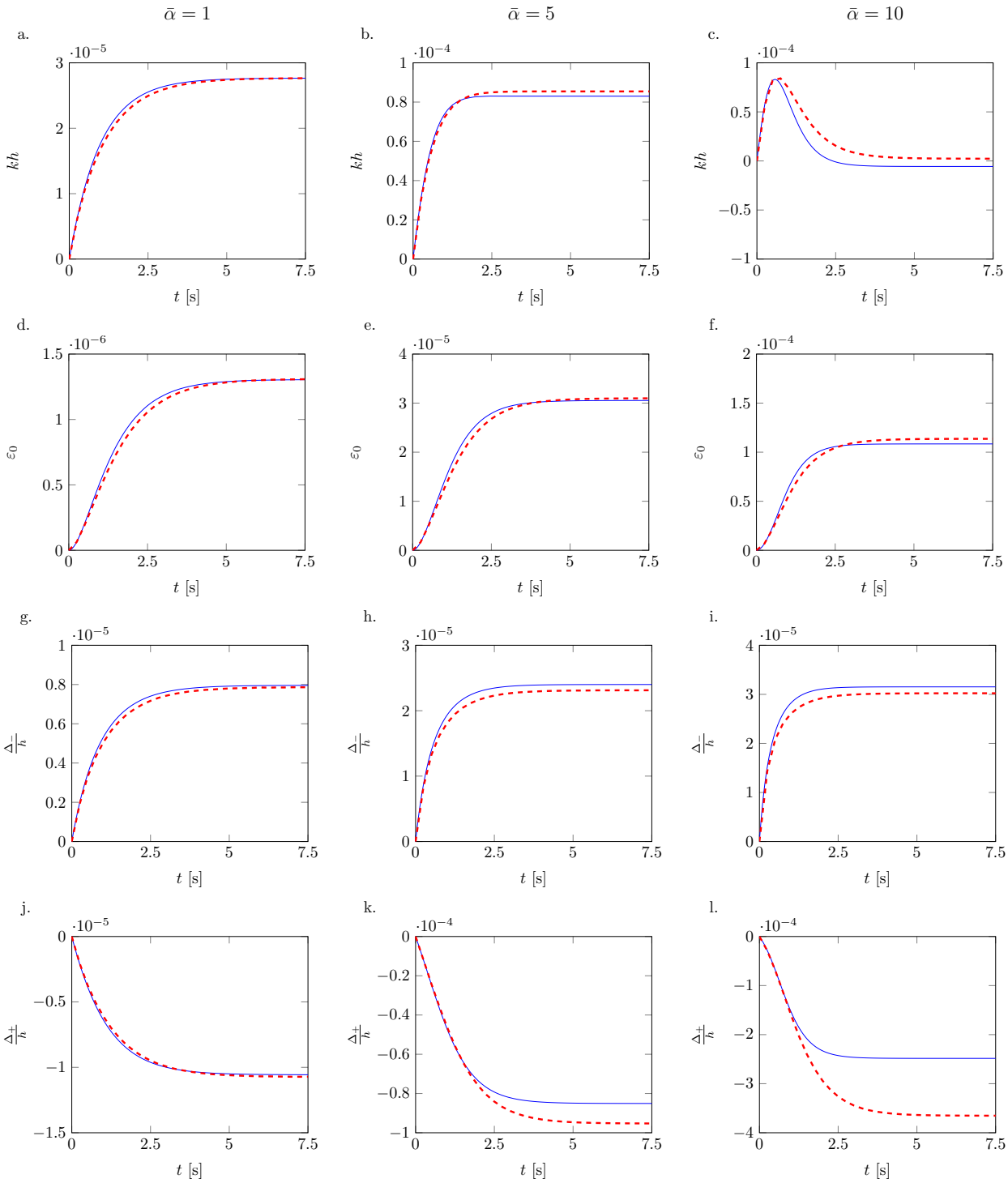

Figure 6: Nondimensional curvature (a, b, and c), mid-axis strain (d, e, and f), and nondimensional displacement of the cathode (g, h, and i) and anode (j, k, and l) with respect to the mid-axis of an IPMC under different step voltages for a Poisson ratio of 0.05. The nondimensional input voltages are 1 (a, d, g, and j), 5 (b, e, h, and k), and 10 (c, f, i, and l). Solid blue lines are the analytical solution, while red dashed lines are FE simulations.

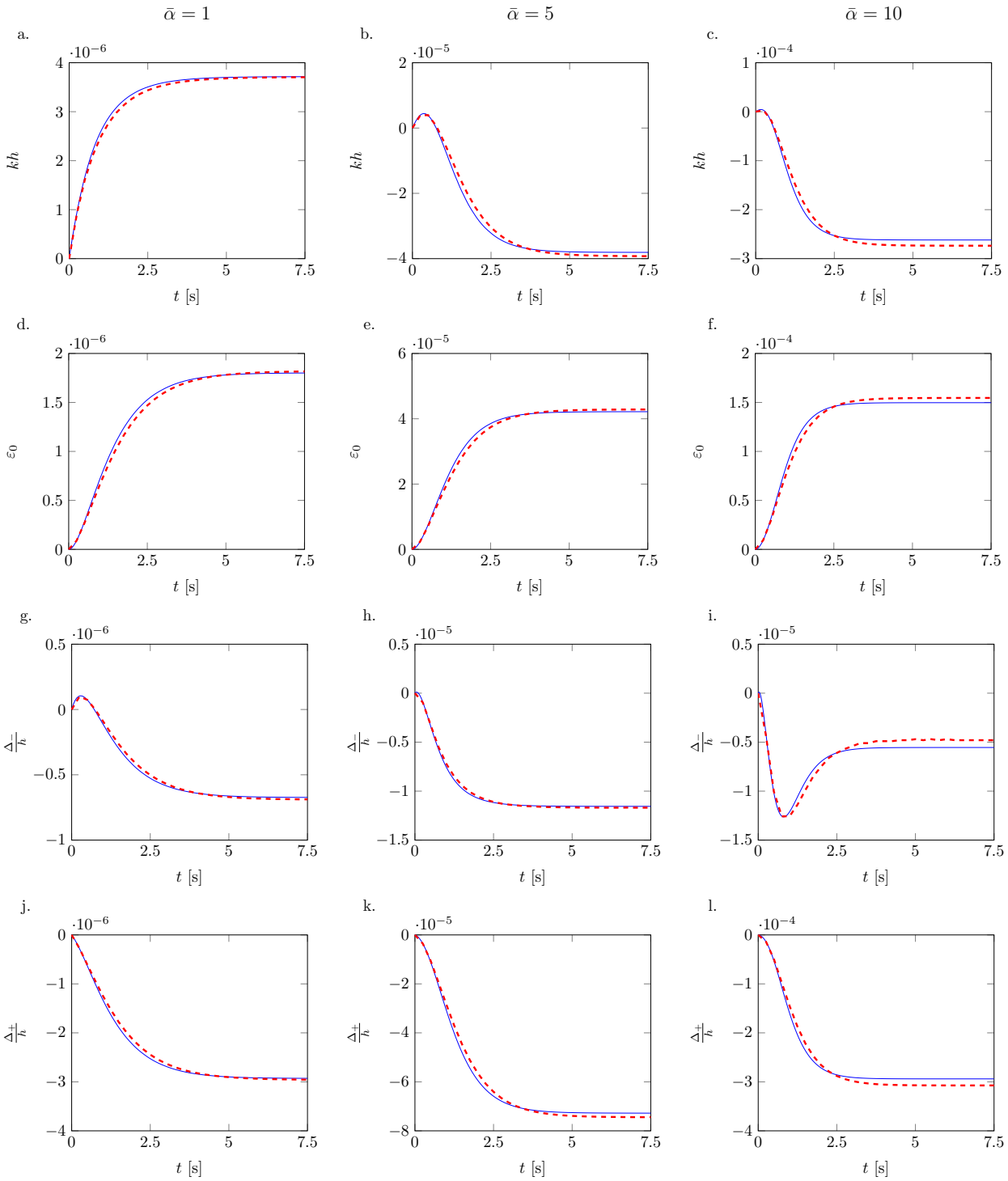

Figure 7: Nondimensional curvature (a, b, and c), mid-axis strain (d, e, and f), and nondimensional displacement of the cathode (g, h, and i) and anode (j, k, and l) with respect to the mid-axis of an IPMC under different step voltages for a Poisson ratio of 0.45. The nondimensional input voltages are 1 (a, d, g, and j), 5 (b, e, h, and k), and 10 (c, f, i, and l). Solid blue lines are the analytical solution, while red dashed lines are FE simulations.

of the deformation that challenges the premise of linear elasticity.

As expected, both the counterions' concentration and the electric potential present an asymmetric double layer structure. The boundary layers show an accumulation of counterions toward the cathode and a corresponding depletion toward the anode. The region of counterion-enrichment toward the cathode has a length of approximately one Debye screening length (corresponding to $\delta = 0.001$ in nondimensional units), while the counterion-depleted region toward the anode is almost three-fold wider. This variation is reflected by the profiles of the electric potential, which show a steeper gradient toward the anode, where it varies from 0 to 5 thermal voltages in almost three Debye screening lengths. The difference in the electric fields toward the two electrodes is the key physical driver of back-relaxation, whereby it controls the value of the contribution to the bending moment due to Maxwell stress, see, for example, Eq. (54c). In the bulk of the ionomer, the counterions' concentration is equal to the concentration of the fixed anions. The voltage, instead, shows a weak linear trend since the solution is not yet at steady-state.

The profiles of the planar components of the strain tensor, namely, the axial, shear, and through-the-thickness strains, are plotted in Figures 10 and 11 for both the Poisson ratios. Consistent with the results on the curvature in Figure 6c, we note a difference in the axial strain between the exact and the FE solution for $\nu = 0.05$, while better agreement is found for $\nu = 0.45$. With respect to the shear strain, FE results confirm our intuition of uniform bending, on which the exact solution was construed. Comparing the predictions of the exact solution with FE findings on through-the-thickness strain, we register a modest underestimation by the exact solution in the case of $\nu = 0.05$, consistent with the severity of the deformation.

FE results confirm the premise of the exact solution that the axial strain is linear in the thickness and does not present any boundary layer. As a result, a beam-like solution for the IPMC deformation, based on the hypothesis of rigid cross-sections, would suffice to capture the axial strain of the IPMC. However, it would be important to include some form of eccentricity, in the form of a mid-axis strain as shown in Eq. (40), which has never been attempted in the technical literature. In fact, the neutral axis, identified as the line on which the axial strain is zero in Figures 10 and 11, does not coincide with the mid-axis, but it is shifted toward the electrodes of more than a quarter of the thickness.

The two-dimensional nature of the problem mostly affects the through-the-thickness strain, as demonstrated by FE simulations and analytical findings. Although almost zero in the bulk of the ionomer, the through-the-thickness strain presents remarkably asymmetric boundary layers. As expected from the discussion in Section 4.3, the anode moves toward the mid-axis, while the cathode moves away from it. Due to the smaller electric field at the cathode, we register a larger through-the-thickness deformation at the anode, where counterions are depleted. For $\nu = 0.05$, the through-the-thickness deformation reaches almost 13% in the proximity of the cathode, which is three orders of magnitude larger than the axial deformation, offering evidence for the importance of multiaxial deformation in IPMCs. A classical beam theory based on rigid cross-sections would fail in predicting this behavior, thereby missing the onset of boundary layers in

the vicinity of the electrodes and the resulting deformation across the thickness during actuation.

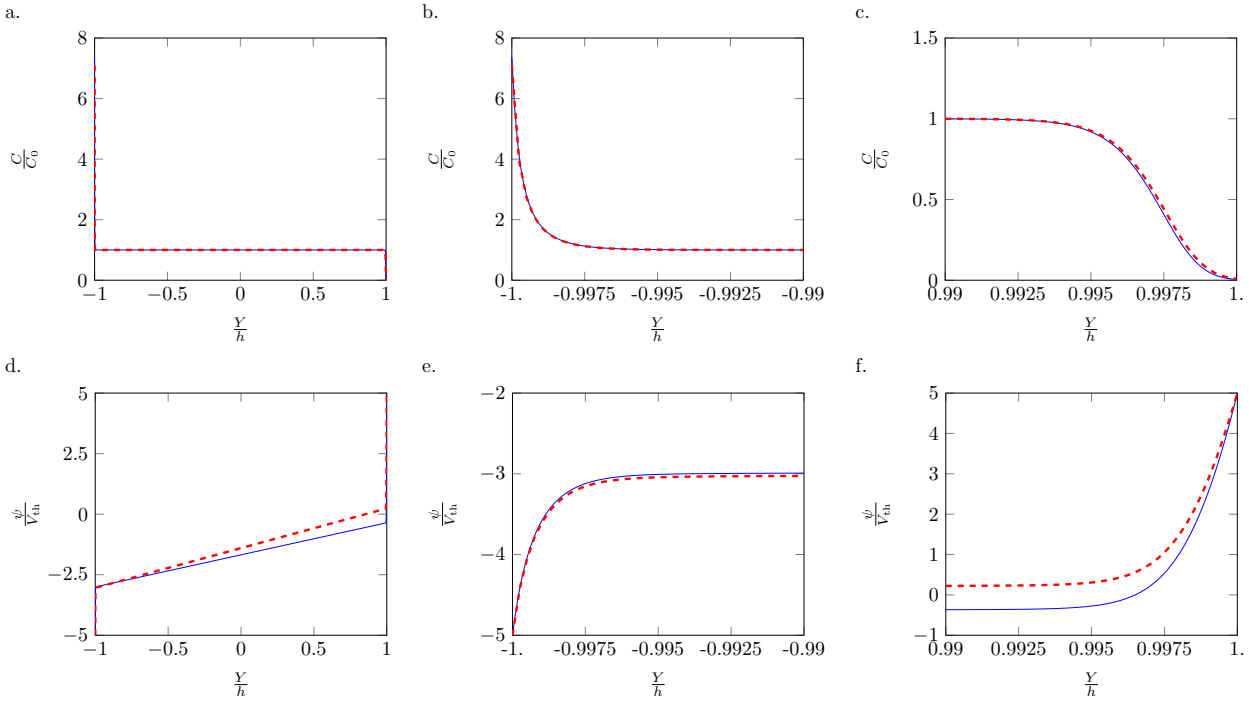

Figure 8: Counterions' concentration (a, b, c) and electric potential (d, e, f) profiles along the thickness at $t^\star = 1$ s for a voltage input of $\bar{\alpha} = 10$ and Poisson ratio of 0.05. The overall profile is shown on the left (a, d). In the central (b, e) and right (c, f) columns, the cathode and anode boundary layer regions are displayed, respectively. Solid blue lines are the analytical solution, while red dashed lines are FE simulations.

6. Conclusions

IPMCs are a novel class of electroactive materials, which are gaining traction as highly-compliant actuators for low-voltage application in wet and dry environments. Despite impressive progress in the technology of IPMC actuators, our comprehension of their physical underpinnings remains elusive. Most of the literature relies on phenomenological models based on reduced-order structural theories (Shahinpoor, 2015; Jo et al., 2013), where actuation is described in terms of an internal, spherical, stress that is proportional to the charge imbalance and the deformation is assumed to follow the classical Euler-Bernoulli beam theory. Here, we examine two-dimensional deformations of an IPMC within a thermodynamically-consistent framework, construed upon a Helmholtz free energy that accounts for mechanical stretching, ion mixing, and dielectric polarization. Through the lens of this continuum model, originally derived in Cha & Porfiri (2014), we study multiaxial deformations of IPMCs, elicited by a complex, nonspherical, internal stress, which is associated with the interplay between osmotic pressure and Maxwell stress.

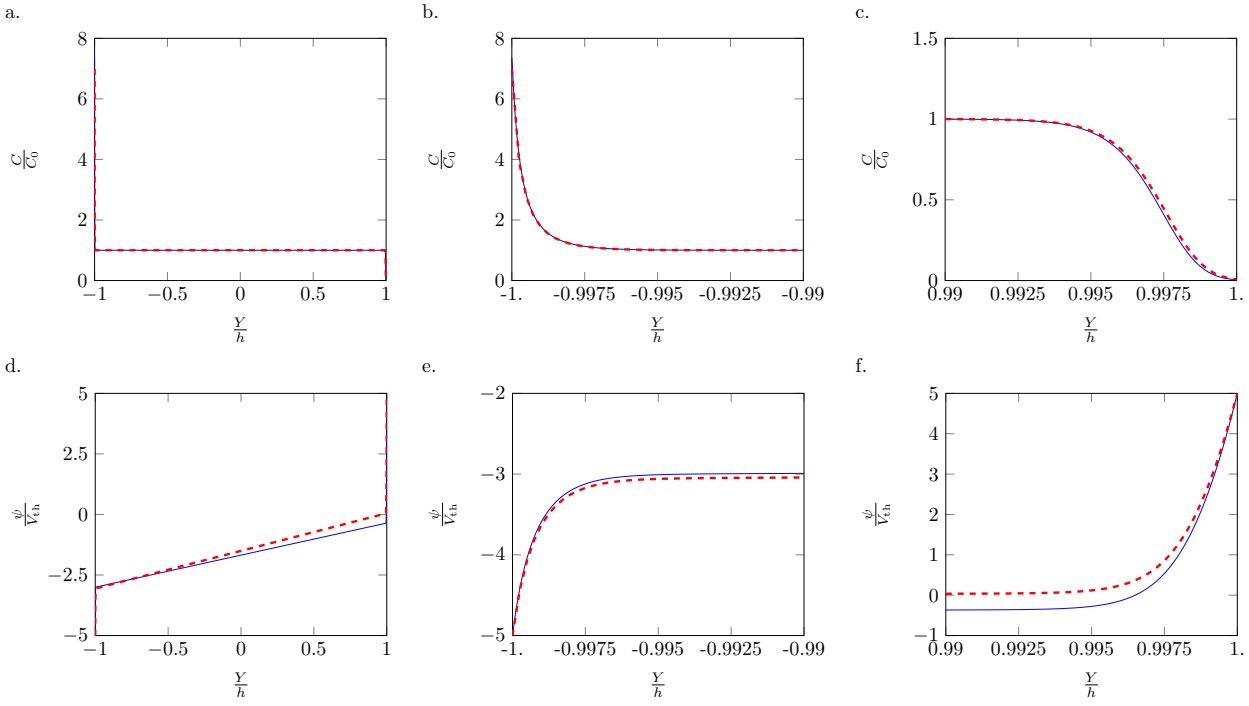

Figure 9: Counterions' concentration (a, b, c) and electric potential (d, e, f) profiles along the thickness at $t^\star = 1$ s for a voltage input of $\bar{\alpha} = 10$ and Poisson ratio of 0.45. The overall profile is shown on the left (a, d). In the central (b, e) and right (c, f) columns, the cathode and anode boundary layer regions are displayed, respectively. Solid blue lines are the analytical solution, while red dashed lines are FE simulations.

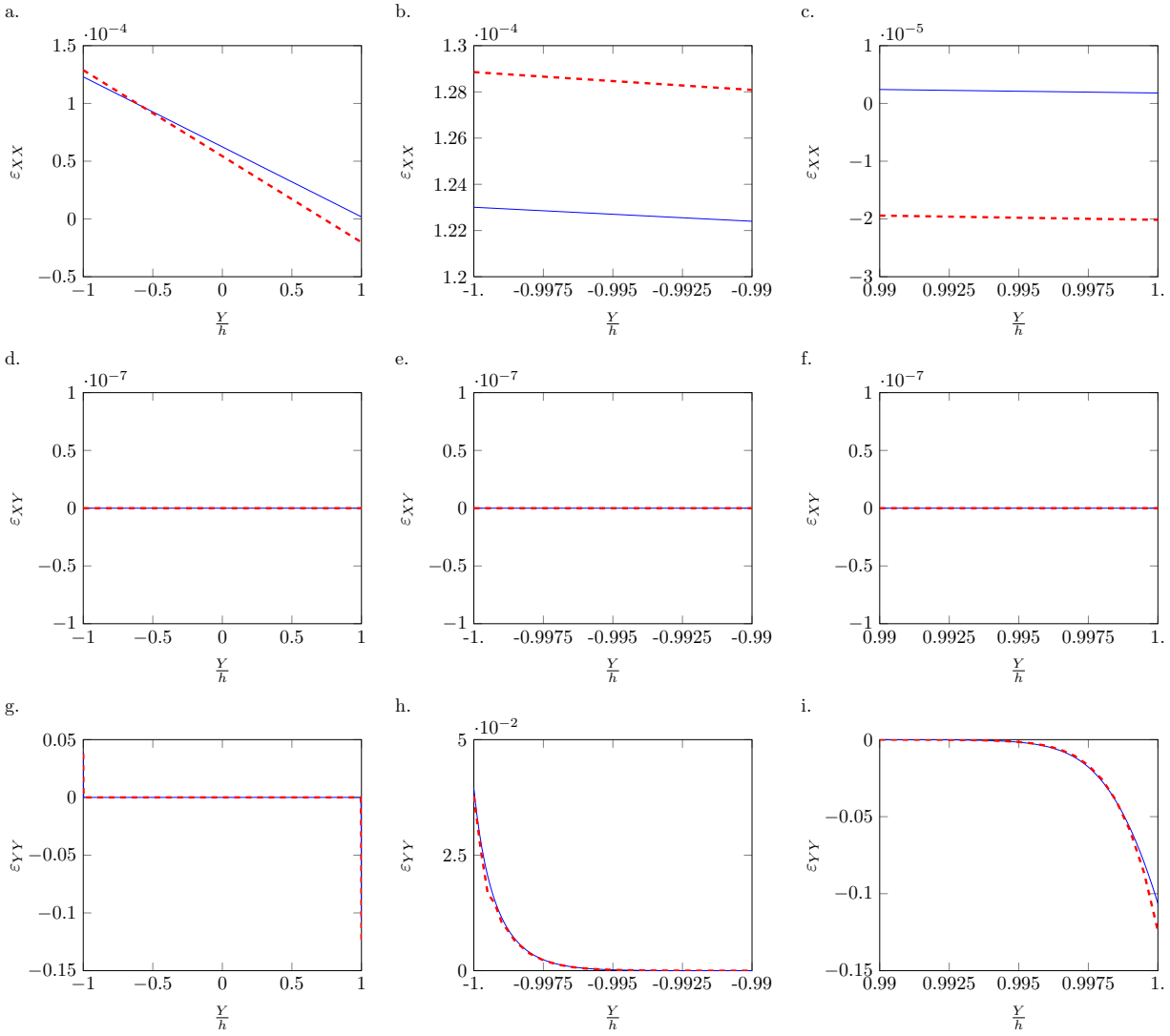

Figure 10: Axial (a, b, c), shear (d, e, f), and through-the-thickness (g, h, i) strain profiles along the thickness at $t^\star = 1$ s for a voltage input of $\bar{\alpha} = 10$ and Poisson ratio of 0.05. The overall profile is shown on the left (a, d, g). In the central (b, e, h) and right (c, f, i) columns, the cathode and anode boundary layer regions are displayed, respectively. Solid blue lines are the analytical solution, while red dashed lines are FE simulations; note that the strain from FE simulations refers to nominal quantities.

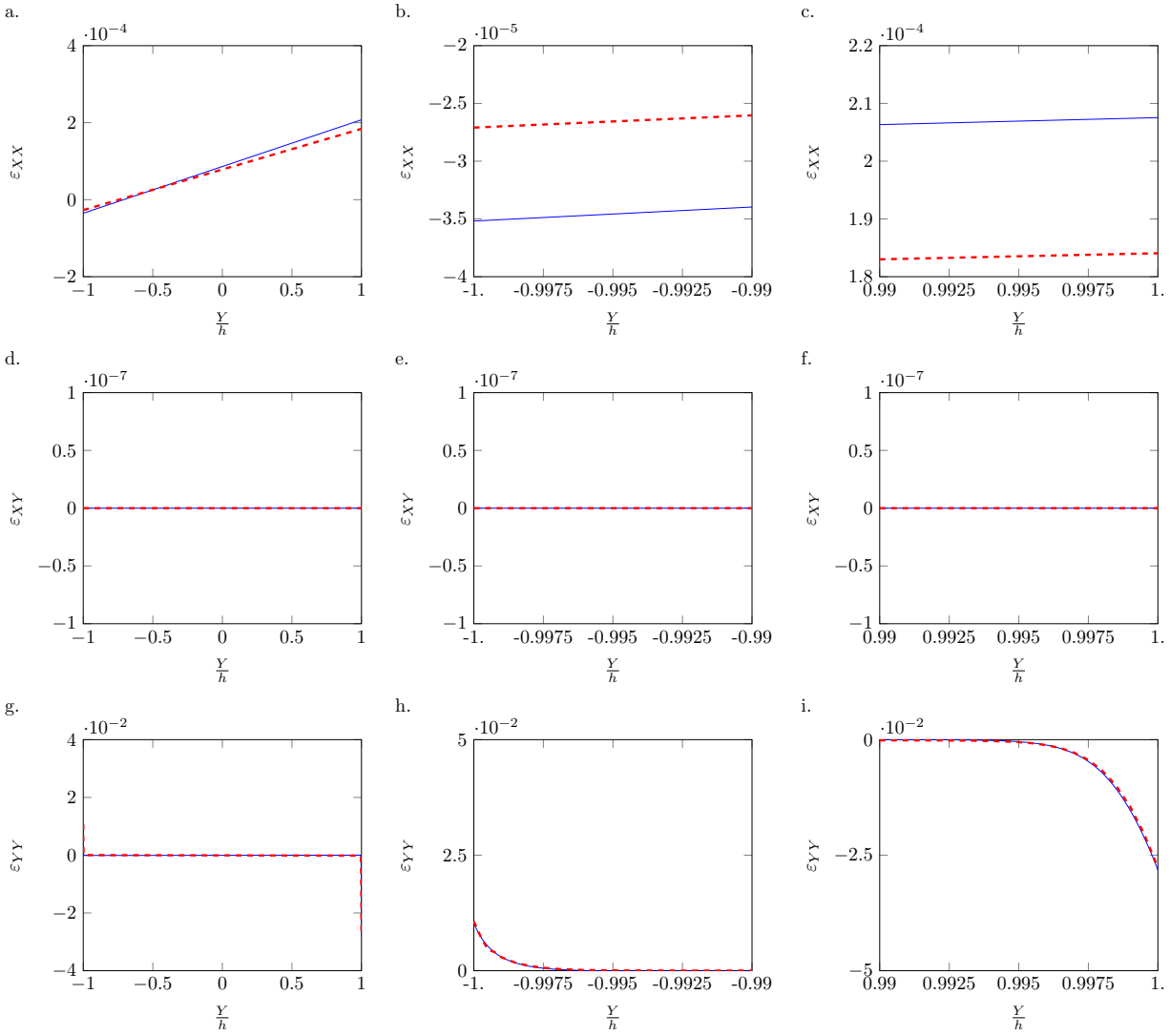

Figure 11: Axial (a, b, c), shear (d, e, f), and through-the-thickness (g, h, i) strain profiles along the thickness at $t^\star = 1$ s for a voltage input of $\bar{\alpha} = 10$ and Poisson ratio of 0.45. The overall profile is shown on the left (a, d, g). In the central (b, e, h) and right (c, f, i) columns, the cathode and anode boundary layer regions are displayed, respectively. Solid blue lines are the analytical solution, while red dashed lines are FE simulations; note that the strain from FE simulations refers to nominal quantities.

We undertake the analysis of the model through two different, complementary perspectives. First, we develop a novel FE simulation environment to implement the proposed continuum IPMC model in the commercial code Abaqus™. Within this computational environment, it is possible to study the nonlinear, fully coupled mechanics and electrochemistry of IPMCs. Second, we establish an exact linear elasticity solution of the problem, by combining the classical Saint-Venant approach to linear elasticity with perturbation methods for resolving the charge double layers at the electrode-ionomer interfaces. This solution builds upon previous work (Porfiri, 2008), which focused exclusively on electrochemistry, to bring new insight on the dependence of the stress within the ionomer on the voltage applied across the electrodes, along with the physical and geometric properties of the actuator.

The analytical perspective allows for a transparent treatment of the problem, which is validated by FE simulations. In general, the exact solution is successful in predicting the complex deformation of IPMCs from the initial bending toward the anode to the back-relaxation toward the cathode. The accuracy of the prediction increases with the value of the Poisson ratio, whereby the exact solution leads to very good quantitative estimations as we approach the incompressible limit. For small values of the Poisson ratio, more severe deformations are attained, thereby challenging the premise of a linear elasticity solution. While axial strains always remain in the linear range, as shown experimentally (Akle & Leo, 2008), through-the-thickness strains reach up to 30% for a voltage of $10\,V_{\mathrm{th}}$, as indicated by FE simulations. In this case, nonlinear terms in the elasticity solution, as well as the coupling between mechanics and electrochemistry, should not be neglected, thereby challenging the computation of an analytical solution. In practice, the severity of these deformations could be mitigated by steric effects (Kilic et al., 2007a,b), which would contain counterions' accumulation toward the cathode. Also, small values of the Poisson ratio are seldom observed in the characterization of ionomers used as core materials in IPMCs (Silberstein & Boyce, 2010; Page et al., 2015; Li & Nemat-Nasser, 2000), thereby suggesting that the practical range of the proposed linear model could be strained beyond our present validation.

Our results offer new evidence of multiaxial deformations of IPMCs during actuation. We discover that the boundary layers in the counterions' concentration and electric potential cause strain localization toward the electrodes. More specifically, the through-the-thickness strain in the IPMC displays an asymmetric strain localization toward the anode and the cathode. Ultimately, this leads to a reduction in the thickness of the IPMC, which is accompanied by a change in the location of its neutral axis and an extension along its length. The Poisson ratio is found to have a critical, unexpected, role on IPMC actuation, which increases as the material approaches the incompressible limit. While the underlying theoretical model has been partially validated through empirical evidence in Cha & Porfiri (2014); Porfiri et al. (2017, 2018), targeted experiments should be designed and conducted to confirm these predictions.

This study, however, does not come without a number of limitations that warrant future research. First, the proposed continuum model does not account for high surface electrodes, which are typically used

in the design of IPMC actuators. Previous work on composite layers (Cha et al., 2012) offers a simple, yet effective methodology to describe the electrochemistry within high surface electrodes. In this vein, each electrode could be modeled as a thick homogeneous layer, with reduced counterions' diffusivity and increased electrical permittivity. While the FE implementation could be readily modified to include composite layers, the analytical solution will require a thorough reexamination, since the hypothesis of null shear deformation is unlikely to be valid everywhere along the cross-section. Perhaps, a potential line of approach could be built upon the seminal work of Pagano (1970) to establish a series solution.

Second, the current continuum model does not explicitly take into consideration the presence of the solvent which is used to hydrate the ionomer and support counterions' motion. Accounting for the presence of the solvent will require the extension of the model kinematics for a separate liquid phase, which could be undertaken within the framework of mixture theory for charged solids in biomechanics (Ateshian, 2007). Again, an analytical treatment of the problem might be difficult, but a FE analysis is likely to be successful.

Finally, the current analysis is limited to two-dimensional deformations, which may not be adequate for describing the response of several IPMC actuators which operate in complex, unstructured environments. Relaxing this assumption should not challenge the development of an analytical solution similar to what we have presented herein, although one should expect bending and stretching on two planes. In this sense, it might even be possible to pursue an exact solution in a nonlinear elastic setting, by focusing on the incompressible limit (Green & Zerna, 1968). On the other hand, establishing a viable FE solution may be challenging, given the computational cost associated with the resolution of the boundary layers close to the electrodes. To date, three-dimensional simulations of double layers are scarce (Rossi & Wallmersperger, 2018).

Beyond addressing these three issues, we envision future endeavors toward the formulation of accurate structural models for IPMC actuators which can capture their complex through-the-thickness response. A first-order displacement-based theory, analogous to the classical Euler-Bernoulli approximation is unlikely to be effective, in that it would not capture the effect of the Poisson ratio on the bending curvature that we have observed in this work. For example, should we set the through-the-thickness deformation to zero, the moment resultants from Maxwell stress and osmotic pressure will be different, thereby leading to an incorrect prediction of the overall bending. This issue may be addressed by exploiting a force-based method or a mixed variational formulation (Teresi & Tiero, 1997), potentially within the context of high-order theories, see, for example, Batra & Vidoli (2002). However, care should be placed to cope with the severity of the deformation of the ionomer toward the electrodes, which we uncovered for small values of the Poisson ratio.

With new advancements in additive manufacturing of IPMCs (Carrico et al., 2017), it becomes of paramount importance to possess predictive modeling tools that could inform the selection of material constituents and the design of complex shapes toward specific objectives. This study makes a first step

in this direction by bringing forward an analytical and computational framework for exploring multiaxial deformations of IPMCs.

Acknowldegments

This research was supported by the National Science Foundation under Grant No. OISE-1545857.

Appendix A. Full expression of the tangent matrices

In this Appendix, we use Einstein convention for indicating the sum over repeated indices. Tangent matrices in Eq. (26) are given by the following integrals:

$$\mathbf{K}^{ij}_{\mathbf{u}_i\mathbf{u}_k} = -\int_{\Omega_{\mathrm{el}}} \frac{\partial N^i}{\partial X_m}\frac{\partial s_{km}}{\partial F_{ln}}\frac{\partial N^j}{\partial X_n}\,\mathrm{d}\Omega, \tag{A.1a}$$

$$\mathbf{K}^{ij}_{\mathbf{u}_k C} = -\int_{\Omega_{\mathrm{el}}} \frac{\partial N^i}{\partial X_l}\frac{\partial s_{kl}}{\partial C}N^j\,\mathrm{d}\Omega, \tag{A.1b}$$

$$\mathbf{K}^{ij}_{\mathbf{u}_k \psi} = -\int_{\Omega_{\mathrm{el}}} \frac{\partial N^i}{\partial X_l}\frac{\partial s_{kl}}{\partial \psi^{\mathrm{k}}}\,\mathrm{d}\Omega, \tag{A.1c}$$

$$\mathbf{K}^{ij}_{C\mathbf{u}_l} = \int_{\Omega_{\mathrm{el}}} \frac{\partial N^i}{\partial X_k}\frac{\partial J_k}{\partial u^j_l}\,\mathrm{d}\Omega, \tag{A.1d}$$

$$K^{ij}_{CC} = -\frac{1}{\Delta t}\int_{\Omega_{\mathrm{el}}} N^i N^j dV + \int_{V_{\mathrm{el}}} \frac{\partial N^i}{\partial X_k}\frac{\partial J_k}{\partial C^j}\,\mathrm{d}\Omega, \tag{A.1e}$$

$$K^{ij}_{C\psi} = \int_{\Omega_{\mathrm{el}}} \frac{\partial N^i}{\partial X_k}\frac{\partial J_k}{\partial \psi^j}\,\mathrm{d}\Omega, \tag{A.1f}$$

$$\mathbf{K}^{ij}_{\psi\mathbf{u}_l} = -\int_{\Omega_{\mathrm{el}}} \frac{\partial N^i}{\partial X_k}\frac{\partial \tilde{D}_k}{\partial F_{lm}}\frac{\partial N^i}{\partial X_m}\,\mathrm{d}\Omega, \tag{A.1g}$$

$$K^{ij}_{\psi C} = -\mathcal{F}\int_{\Omega_{\mathrm{el}}} N^i N^j\,\mathrm{d}\Omega, \tag{A.1h}$$

$$K^{ij}_{\psi\psi} = -\int_{\Omega_{\mathrm{el}}} \frac{\partial N^i}{\partial X_k}\frac{\partial \tilde{D}_k}{\partial \psi^j}\,\mathrm{d}\Omega. \tag{A.1i}$$

Here, Δt is the time step used by the implicit solver in Abaqus™.

References

Akle, B. J., Bennett, M. D., Leo, D. J., Wiles, K. B., & McGrath, J. E. (2007). Direct assembly process: A novel fabrication technique for large strain ionic polymer transducers. *Journal of Materials Science*, *42*, 7031 – 7041. doi:https://doi.org/10.1007/s10853-006-0632-4.

Akle, B. J., Habchi, W., Wallmersperger, T., Akle, E. J., , & Leo, D. J. (2011). High surface area electrodes in ionic polymer transducers: Numerical and experimental investigations of the electro-chemical behavior. *Journal of Applied Physics*, *109*. doi:https://doi.org/10.1063/1.3556751.

Akle, B. J., & Leo, D. J. (2008). Single–walled carbon nanotubes – ionic polymer electroactive hybrid transducers. *Journal of Intelligent Material Systems and Structures*, *19*. doi:https://doi.org/10.1177\%2F1045389X07082441.

Asaka, K., Oguro, K., Nishimura, Y., Mizuhata, M., & Takenaka, H. (1995). Bending of polyelectrolyte membrane-platinum composites by electric stimuli I. Response characteristics to various waveforms. *Polymer Journal*, *27*, 436–440. doi:https://doi.org/10.1295/polymj.27.436.

Ateshian, G. A. (2007). On the theory of reactive mixtures for modeling biological growth. *Biomechanics and Modeling in Mechanobiology*, *6*, 423–445. doi:https://doi.org/10.1007/s10237-006-0070-x.

Aureli, M., Kopman, V., & Porfiri, M. (2010). Free-locomotion of underwater vehicles actuated by ionic polymer metal composites. *IEEE/ASME Transactions on Mechatronics*, *15*, 603–614. doi:https://doi.org/10.1109/TMECH.2009.2030887.

Bard, A. J., & Faulkner, L. R. (2001). *Electrochemical Methods - Fundamentals and Applications*. John Wiley & Sons.

Batra, R. C. (2001). Comparison of results from four linear constitutive relations in isotropic finite elasticity. *International Journal of Non-Linear Mechanics*, *36*, 421–432. doi:https://doi.org/10.1016/S0020-7462(00)00057-3.

Batra, R. C., & Vidoli, S. (2002). Higher-order piezoelectric plate theory derived from a three-dimensional variational principle. *AIAA Journal*, *40*, 91–104. doi:https://doi.org/10.2514/2.1618.

Belytschko, T., Liu, W. K., Moran, B., & Elkhodary, K. I. (2014). *Nonlinear Finite Elements for Continua and Structures*. (2nd ed.). Wiley.

Bhandari, B., Lee, G.-Y., & Ahn, S.-H. (2012). A review on IPMC material as actuators and sensors: Fabrications, characteristics and applications. *International Journal of Precision Engineering and Manufacturing*, *13*, 141–163. doi:https://doi.org/10.1007/s12541-012-0020-8.

Carrico, J. D., Tyler, T., & Leang, K. K. (2017). A comprehensive review of select smart polymeric and gel actuators for soft mechatronics and robotics applications: fundamentals, freeform fabrication, and motion control. *International Journal of Smart and Nano Materials*, *8*, 144–213. doi:https://doi.org/10.1080/19475411.2018.1438534.

Cha, Y., Aureli, M., & Porfiri, M. (2012). A physics-based model of the electrical impedance of ionic polymer metal composites. *Journal of Applied Physics*, *111*. doi:https://doi.org/10.1063/1.4729051.

Cha, Y., & Porfiri, M. (2014). Mechanics and electrochemistry of ionic polymer metal composites. *Journal of the Mechanics and Physics of Solids*, *71*, 156–178. doi:https://doi.org/10.1016/j.jmps.2014.07.006.

Chen, J., Yu, P., Wang, H., Liew, K. M., & Shen, S. (2018). An ABAQUS implementation of electrochemomechanical theory for mixed ionic electronic conductors. *Solid State Ionics*, *319*, 34–45. doi:https://doi.org/10.1016/j.ssi.2018.01.043.

Chen, Z. (2017). A review on robotic fish enabled by ionic polymer-–metal composite artificial muscles. *Robotics and Biomimetics*, *4*. doi:https://doi.org/10.1186/s40638-017-0081-3.

Chen, Z., Shatara, S., & Tan, X. (2009). Modeling of biomimetic robotic fish propelled by an ionic polymer—metal composite caudal fin. *IEEE/ASME Transactions on Mechatronics*, *15*, 448–459. doi:https://doi.org/10.1109/TMECH.2009.2027812.

Chen, Z., & Tan, X. (2008). A control-oriented and physics-based model for ionic polymer-metal composite actuators. *IEEE/ASME Transactions on Mechatronics*, *13*, 519–529. doi:https://doi.org/10.1109/TMECH.2008.920021.

Chen, Z., Um, T. I., & Bart-Smith, H. (2012). Bio-inspired robotic manta ray powered by ionic polymer-–metal composite

artificial muscles. *International Journal of Smart and Nano Materials*, *3*, 296–308. doi:https://doi.org/10.1080/19475411.2012.686458.

Chester, S. A., Di Leo, C. V., & Anand, L. (2015). A finite element implementation of a coupled diffusion-deformation theory for elastomeric gels. *International Journal of Solids and Structures*, *52*, 1–18. doi:http://dx.doi.org/10.1016/j.ijsolstr.2014.08.015.

Del Bufalo, G., Placidi, L., & Porfiri, M. (2008). A mixture theory framework for modeling the mechanical actuation of ionic polymer metal composites. *Smart Materials and Structures*, *17*. doi:{https://doi.org/10.1088/0964-1726/17/4/045010}.

Fried, I. (1974). Numerical integration in the finite element method. *Computers & Structures*, *4*, 921–932. doi:https://doi.org/10.1016/0045-7949(74)90015-7.

Giner, E., Sukumar, N., Tarancón, J. E., & Fuenmayor, F. J. (2009). An Abaqus implementation of the extended finite element method. *Engineering Fracture Mechanics*, *76*, 347–368. doi:https://doi.org/10.1016/j.engfracmech.2008.10.015.

Green, A. E., & Zerna, W. (1968). *Theoretical elasticity*. (2nd ed.). Dover.

Gurtin, M. E., Fried, E., & Anand, L. (2013). *The Mechanics and Thermodynamics of Continua*. Cambridge University Press.

Hong, W., Zhao, X., & Suo, Z. (2010). Large deformation and electrochemistry of polyelectrolyte gels. *Journal of the Mechanics and Physics of Solids*, *58*, 558–577. doi:https://doi.org/10.1016/j.jmps.2010.01.005.

Jo, C., Pugal, D., Oh, I.-K., Kim, K. J., & Asaka, K. (2013). Recent advances in ionic polymer—metal composite actuators and their modeling and applications. *Progress in Polymer Science*, *38*, 1037–1066. doi:https://doi.org/10.1016/j.progpolymsci.2013.04.003.

Johanson, U., Punning, A., & Aabloo, A. (2015). Ionic polymer metal composites with electrochemically active electrodes. In M. Shahinpoor (Ed.), *Ionic Polymer Metal Composites (IPMCs): Smart Multi-Functional Materials and Artificial Muscles* (pp. 215–227). Royal Society of Chemistry volume 1. doi:http://dx.doi.org/10.1039/9781782622581.

Kilic, M. S., Bazant, M. Z., & Ajdari, A. (2007a). Steric effects in the dynamics of electrolytes at large applied voltages. I. Double-layer charging. *Physical Review E*, *75*. doi:https://doi.org/10.1103/PhysRevE.75.021502.

Kilic, M. S., Bazant, M. Z., & Ajdari, A. (2007b). Steric effects in the dynamics of electrolytes at large applied voltages. II. Modified Poisson-Nernst-Planck equations. *Physical Review E*, *75*. doi:https://doi.org/10.1103/PhysRevE.75.021503.

Kim, B., Kim, D.-H., Jung, J., & Park, J.-O. (2005). A biomimetic undulatory tadpole robot using ionic polymer-metal composite actuators. *Smart Materials and Structures*, *14*. doi:https://doi.org/10.1088/0964-1726/14/6/051.

Kim, K. J., Palmre, V., Stalbaum, T., Hwang, T., Shen, Q., & Trabia, S. (2016). Promising developments in marine applications with artificial muscles: Electrodeless artificial cilia microfibers. *Marine Technology Society*, *50*, 24–34. doi:https://doi.org/10.4031/MTSJ.50.5.4.

Lapidus, L., & Pinder, G. F. (2011). *Numerical Solution of Partial Differential Equations in Science and Engineering*. Wiley. doi:10.1002/9781118032961.

Li, J. Y., & Nemat-Nasser, S. (2000). Micromechanical analysis of ionic clustering in Nafion perfluorinated membrane. *Mechanics of Materials*, *32*, 303–314. doi:https://doi.org/10.1016/S0167-6636(00)00002-8.

Najem, J., Sarles, S. A., Akle, B., & Leo, D. J. (2012). Biomimetic jellyfish-inspired underwater vehicle actuated by ionic polymer metal composite actuators. *Smart Materials and Structures*, *21*. doi:https://doi.org/10.1088/0964-1726/21/9/094026.

Nardinocchi, P., Pezzulla, M., & Placidi, L. (2011). Thermodynamically based multiphysic modeling of ionic polymer metal composites. *Journal of Intelligent Material Systems and Structures*, *22*, 1887–1897. doi:https://doi.org/10.1177\%2F1045389X11417195.

Nemat-Nasser, S., & Li, J. Y. (2000). Electromechanical response of ionic polymer-metal composites. *Journal of Applied Physics*, *87*. doi:https://doi.org/10.1063/1.372343.

Oguro, K. (Retrieved on August 10, 2018). Preparation procedure - Ion-exchange polymer metal composites (IPMC) mem-

branes. URL: https://ndeaa.jpl.nasa.gov/nasa-nde/lommas/eap/IPMC_PrepProcedure.htm.

Pagano, N. J. (1970). Exact solutions for rectangular bidirectional composites and sandwich plates. *Journal of Composite Materials*, *4*, 20–34. doi:https://doi.org/10.1177\%2F002199837000400102.

Page, K. A., Shin, J. W., Eastman, S. A., Rowe, B. W., Kim, S., Kusoglu, A., Yager, K. G., & Stafford, G. R. (2015). In situ method for measuring the mechanical properties of nafion thin films during hydration cycles. *ACS Applied Materials & Interfaces*, *7*, 17874—-17883. doi:10.1021/acsami.5b04080.

Park, I.-S., Kim, S.-M., Pugal, D., Huang, L., Tam-Chang, S.-W., & Kim, K. J. (2010). Visualization of the cation migration in ionic polymer-metal composite under an electric field. *Applied Physics Letters*, *96*. doi:https://doi.org/10.1063/1.3293290.

Park, K., & Paulino, G. H. (2012). Computational implementation of the PPR potential-based cohesive model in ABAQUS: Educational perspective. *Engineering Fracture Mechanics*, *93*, 239–262. doi:https://doi.org/10.1016/j.engfracmech.2012.02.007.

Porfiri, M. (2008). Charge dynamics in ionic polymer metal composites. *Journal of Applied Physics*, *104*. doi:https://doi.org/10.1063/1.3017467.

Porfiri, M. (2009). Influence of electrode surface roughness and steric effects on the nonlinear electromechanical behavior of ionic polymer metal composites. *Physical Review E*, *79*. doi:https://doi.org/10.1103/PhysRevE.79.041503.

Porfiri, M., Leronni, A., & Bardella, L. (2017). An alternative explanation of back-relaxation in ionic polymer metal composites. *Extreme Mechanics Letters*, *13*, 78–83. doi:https://doi.org/10.1016/j.eml.2017.01.009.

Porfiri, M., Sharghi, H., & Zhang, P. (2018). Modeling back-relaxation in ionic polymer metal composites: The role of steric effects and composite layers. *Journal of Applied Physics*, *123*. doi:https://doi.org/10.1063/1.5004573.

Pugal, D., Solin, P., Kim, K. J., & Aabloo, A. (2014). hp-FEM electromechanical transduction model of ionic polymer–metal composites. *Journal of Computational and Applied Mathematics*, *260*, 135–148. doi:https://doi.org/10.1016/j.cam.2013.09.011.

Pugal, D., Stalbaum, T., Palmre, V., & Kim, K. J. (2015). Modeling ionic polymer metal composites with COMSOL: Step-by-step guide. In *Ionic Polymer Metal Composites (IPMCs): Smart Multi-Functional Materials and Artificial Muscles* (pp. 185–214). Royal Society of Chemistry volume 1. doi:http://dx.doi.org/10.1039/9781782622581.

Reese, S., & Wriggers, P. (2000). A stabilization technique to avoid hourglassing in finite elasticity. *International Journal for Numerical Methods in Engineering*, *48*, 79–109. doi:https://doi.org/10.1002/(SICI)1097-0207(20000510)48:1\%3C79::AID-NME869\%3E3.0.CO;2-D.

Rossi, M., & Wallmersperger, T. (2018). Thermodynamically consistent three-dimensional electrochemical model for polymeric membranes. *Electrochimica Acta*, *283*, 1323–1338. doi:https://doi.org/10.1016/j.electacta.2018.06.174.

Shahinpoor, M. (Ed.) (2015). *Ionic Polymer Metal Composites (IPMCs): Smart Multi-Functional Materials and Artificial Muscles*. Smart Materials Series. Royal Society of Chemistry. doi:http://dx.doi.org/10.1039/9781782622581.

Shahinpoor, M., & Kim, K. J. (2002). Mass transfer induced hydraulic actuation in ionic polymer-metal composites. *Journal of Intelligent Material Systems and Structures*, *13*, 369–376. doi:https://doi.org/10.1177\%2F104538902761696715.

Shahinpoor, M., & Kim, K. J. (2004). Ionic polymer–metal composites: IV. Industrial and medical applications. *Smart Materials and Structures*, *14*. doi:https://doi.org/10.1088/0964-1726/14/1/020.

Shen, Q., Palmre, V., Stalbaum, T., & Kim, K. J. (2015). A comprehensive physics-based model encompassing variable surface resistance and underlying physics of ionic polymer-metal composite actuators. *Journal of Applied Physics*, *118*. doi:https://doi.org/10.1063/1.4931912.

Silberstein, M. N., & Boyce, M. C. (2010). Constitutive modeling of the rate, temperature, and hydration dependent deformation response of Nafion to monotonic and cyclic loading. *Journal of Power Sources*, *195*, 5692–5706. doi:https://doi.org/10.1016/j.jpowsour.2010.03.047.

de Souza Neto, E. A., Perić, D., Dutko, M., & Owen, D. R. J. (1996). Design of simple low order finite elements for large

strain analysis of nearly incompressible solids. *International Journal of Solids and Structures*, *33*, 3277–3296. doi:https://doi.org/10.1016/0020-7683(95)00259-6.

Stalbaum, T., Hwang, T., Trabia, S., Shen, Q., Hunt, R., Olsen, Z., & Kim, K. J. (2017). Bioinspired travelling wave generation in soft-robotics using ionic polymer-metal composites. *International Journal of Intelligent Robotics and Applications*, *1*, 167–179. doi:https://doi.org/10.1007/s41315-017-0015-9.

Teresi, L., & Tiero, A. (1997). On variational approaches to plate modes. *Meccanica*, *32*, 143–156. doi:https://doi.org/10.1023/A:1004271405217.

Thornton, E. A. (1996). *Thermal Structures for Aerospace Applications*. AIAA Education Series. American Institute of Aeronautics and Astronautics. doi:https://doi.org/10.2514/4.862540.

Timoshenko, S., & Goodier, J. (2001). *Theory of Elasticity*. (3rd ed.). McGrawHill.

Wallmersperger, T., Leo, D. J., & Kothera, C. S. (2007). Transport modeling in ionomeric polymer transducers and its relationship to electromechanical coupling. *Journal of Applied Physics*, *101*. doi:https://doi.org/10.1063/1.2409362.

Yeom, S.-W., & Oh, I.-K. (2009). A biomimetic jellyfish robot based on ionic polymer metal composite actuators. *Smart Materials and Structures*, *18*. doi:https://doi.org/10.1088/0964-1726/18/8/085002.

Zhu, Z., Asaka, K., Chang, L., Takagi, K., & Chen, H. (2013). Multiphysics of ionic polymer-metal composite actuator. *Journal of Applied Physics*, *114*. doi:https://doi.org/10.1063/1.4818412.

Zienkiewicz, O., & Taylor, R. (2013). *The finite element method*. (Seventh ed.). ButterworthHeinemann.